

Effects of Particle and Environmental Variables on  
Rheology and Interaction of Granular Materials

by

Spandana Vajrala

A Dissertation Presented in Partial Fulfillment  
of the Requirements for the Degree  
Doctor of Philosophy

Approved April 2021 by the  
Graduate Supervisory Committee:

Heather Emady, Chair  
Hamid Marvi  
Yang Jiao

ARIZONA STATE UNIVERSITY

May 2021

## ABSTRACT

Granular materials demonstrate complexity in many physical attributes with various shapes and sizes, varying from several centimeters down to less than a few microns. Some materials are highly cohesive, while others are free-flowing. Despite such complexity in their physical properties, they are extremely important in industries dealing with bulk materials. Through this research, the factors affecting flowability of particulate solids and their interaction with projectiles were explored.

In Part I, a novel set of characterization tools to relate various granular material properties to their flow behavior in confined and unconfined environments was investigated. Through this work, a thorough characterization study to examine the effects of particle size, particle size distribution, and moisture on bulk powder flowability were proposed. Additionally, a mathematical model to predict the flow function coefficient (FFC) was developed, based on the surface mean diameter and moisture level, which can serve as a flowability descriptor.

Part II of this research focuses on the impact dynamics of low velocity projectiles on granular media. Interaction of granular media with external foreign bodies occurs in everyday events like a human footprint on the beach. Several studies involving numerical and experimental methods have focused on the study of impact dynamics in both dry and wet granular media. However, most of the studies involving impact dynamics considered spherical projectiles under different conditions, while practical models should involve more complex, realistic shapes. Different impacting geometries with conserved density, volume, and velocity on a granular bed may experience contrasting drag forces upon penetration. This is due to the difference in the surface areas coming into contact with the

granular media. In this study, a set of non-spherical geometries comprising cuboids, cylinders, hexagonal prisms and triangular prisms with constant density, volume, and impact velocities, were released onto a loosely packed, non-cohesive, dry granular bed. From these experimental results, a model to determine the penetration depth of projectiles upon impact was developed and how it is influenced by the release height and surface area of the projectiles in contact with the granular media was studied.

To my family

## ACKNOWLEDGMENTS

My deep gratitude goes first to Dr. Heather Emady, for her affable and encouraging guidance throughout the course of my research. Her knowledge and unwavering enthusiasm for my field of research kept me constantly engaged. Her personal generosity helped me make my time at ASU enjoyable.

I would also like to thank my committee, Dr. Hamid Marvi and Dr. Yang Jiao for their valuable support and collaboration in my research. I am also grateful to the Arizona State University, as it provided me with an opportunity to align myself with my current research and to know more about this phase of work.

My appreciation extends to my colleagues, Tianxiang, Manogna and Bhaumik for their close collaboration and feedback throughout these years. I must thank Radhalakshmi and Anindya for their invaluable help during the final year of my PhD. I wish to thank all the graduate and undergraduate students who generously assisted me in performing experiments in the lab.

It is a pleasure to thank Dr. Quang Nyugen for helping me gain new insight into my research. We would also like to acknowledge Idaho National Laboratory for its support and collaboration. I am grateful to Applied Materials for funding the final year of my PhD and providing me an opportunity to expand the scope of my research to new applications and projects.

Thank you Manogna, for being an amazing lab mate and roommate over the years! All the trips and activities we did together made me forget home. Saketh, you are such a light!

Your positivity and kindness made my time so much better and thank you for all those musical moments. Thank you to all my friends in Tempe for making my stay a breeze.

Above ground, I am indebted to my family for the support and unconditional love given to me. Bannu, I am ever grateful for being your sister. You are a true inspiration! Mom and dad, you are simply the best parents anyone could dream of. Your constant encouragement and trust gave me the strength to keep up my studies.

## TABLE OF CONTENTS

CHAPTER	Page
LIST OF TABLES .....	viii
LIST OF FIGURES .....	ix
CHAPTER 1 INTRODUCTION.....	1
Section 1.1. Flowability.....	2
Section 1.2. Common flow issues .....	3
Section 1.3. Thesis Objectives .....	4
CHAPTER 2 LITERATURE REVIEW .....	7
Section 2.1. A summary of conventional flowability descriptors.....	10
Section 2.2. Literature review on impact of projectiles on granular media.....	15
CHAPTER 3 MATERIALS AND METHODOLOGY .....	19
Section 3.1. Materials .....	19
Section 3.2. Material preparation .....	19
Section 3.3. Characterization methods.....	20
Section 3.4. Particle Characterization .....	23
Section 3.5. Flowability experiments.....	24
Section 3.6. Impact experiments - methodology .....	32
CHAPTER 4. EFFECT OF PARTICLE AND ENVIRONMENTAL VARIABLES ON RHEOLOGY OF GRANULAR MATERIALS .....	35
Section 4.1. Angle of repose .....	35
Section 4.2. Conditioned bulk density .....	36
Section 4.3. Compressibility measurements .....	37

CHAPTER	Page
Section 4.4. Basic flowability energy (BFE) .....	38
Section 4.5. Specific energy (SE) .....	39
Section 4.6. Shear cell measurements .....	43
<b>CHAPTER 5. IMPACT OF NON-SPHERICAL PROJECTILES ON DRY</b>	
<b>GRANULAR MEDIA.....</b>	<b>54</b>
Section 5.1. Results and discussion.....	54
<b>CHAPTER 6 CONCLUSIONS AND FUTURE WORK.....</b>	<b>62</b>
Section 6.1. Flowability Quantification of Glass Beads.....	62
Section 6.2. Projectile Impacts on Granular Media.....	63
<b>REFERENCES .....</b>	<b>65</b>
<b>APPENDIX</b>	
<b>A FLOWABILITY DATA COLLECTED FOR BIOMASS SAMPLES .....</b>	<b>73</b>
<b>B RAW DATA AND STATISTICAL ANALYSIS FOR IMPACT</b>	
<b>EXPERIMENTS .....</b>	<b>80</b>



## LIST OF TABLES

Table	Page
1. Types of Flow Patterns in Silos and Hoppers .....	13
2. A Summary of Conventional Flowability Descriptors for Granular Material .....	18
3. Carr Index, Hausner Ratio, and FFC values to Quantitatively Describe the Nature of Bulk Materials .....	23
4. Experimental Parameters, Including Geometrical and Physical Properties of the Projectiles and the Granular Target. <i>L</i> and <i>A</i> Represent Vertical Height and Cross-sectional Area of the Shapes, Respectively .....	46
5. Density-Based Flowability Descriptors of the Materials Used in the Study .....	49
6. a) Results from the Shear Cell Tests of the Bulk Solids that were used in the Study, Averaged Over 3 Runs for Each Particle Size Range and Moisture Content Combination. The Standard Deviation of the Average Values of FFC is also shown .....	56
b) Results from the Shear Cell Test of Bulk Solids that were Excluded from the Study After Initial Testing, Averaged Over 3 Runs for Each Particle Size Range and Moisture Content Combination. The Standard Deviation of the Average Values of FFC is also shown .....	57
Appendix Table	
B.1. Raw data for Penetration Depth of Non-Spherical Geometries Used in the Study .....	80

LIST OF FIGURES

Figure	Page
<i>Figure 1.</i> Classification of Flow Issues. (Baxter & Prescott, 2017).....	4
<i>Figure 2.</i> Steps Involving Antistatic Solution Treatment .....	20
<i>Figure 3</i> (a) Angle of Repose Apparatus; (b) Sample Image of the Heap Formed Using the Aor Apparatus .....	21
<i>Figure 4(A).</i> Sample Angle of Repose Picture; (b) & (c) Images Depicting how the Angle Tool is Used to Draw Lines in ImageI.....	22
<i>Figure 5.</i> Imagej Menu Bar With Angle Tool Selected .....	23
<i>Figure 6.</i> A Schematic of Impeller Inside the Powder Column in the FT4 Rheometer. Work Done by the Blade For Each Millimeter Travelled in the Entire Column is Calculated by the Instrument Using Force and Torque Values, and an Energy Gradient is Determined. Consequently, the TE is Represented by the Area Under the Energy Gradient Curve (Right). The Image on the Left Shows the Total Distance Travelled by The Impeller Through the Powder Column From H1 To H2. (FT4 Powder Rheometer - Dynamic Methodology, N.D.).....	26
<i>Figure 7.</i> The Vessel Used For the Shear Cell Test on the FT4. The Splitting Mechanism is Used to Get Rid of the Excess Material, Resulting in and we are Left With a Flat Surface For the Experiment. ....	28
<i>Figure 8.</i> Successive Shearing Operations Done in a Single Shear Cell Test Experiment. The Bottom Curves are the Shear Stress Plots, With Peaks Representing the Point of Incipient Flow (Shear Test Points) Corresponding to Each Normal Stress Value Plotted On Top.....	29

**Figure 9.** The Construction Of Yield Locus And The Mohr's Circles. The Values Obtained From The Intercepts Of The Circles Are Used To Calculate The Flow Function Coefficient..... 30

**Figure 10.** (A) 309.90  $\mu\text{m}$  Particle Size, 0.5% Moisture Content. Displaying The Pendular State. Liquid Bridges Can Be Seen Forming Between The Glass Beads. The Bonding Energy From The Liquid Bridges Keeps The Beads Together. (B) 309.90  $\mu\text{m}$  Particle Size, 1% Moisture Content. Displaying The Pendular State. (C) 309.9  $\mu\text{m}$  Particle Size, 5% Moisture Content. Displaying The Pendular State. Volume Of Liquid Bridges Increasing Further. As The Volume Increases, The Bonding Strength Increases, And The Beads Are Packed Closer. (D) 309.9  $\mu\text{m}$  Particle Size, 10% Moisture Content. Displaying The Funicular State. Due To The Increasing Volume Content, The Liquid Bridges Start Filling Up The Void In Between The Glass Beads. The Surface Tension Starts Playing A Part In Keeping The Beads Together. (E) 309.9  $\mu\text{m}$  Particle Size, 15% Moisture Content. Mixture Transitioned Into Capillary State. The Bonding Strength Between The Glass Beads Is Now Affected By The Capillary Pressure Of The Liquid Content Of The Bulk Solid. .... 31

**Figure 11(A)** 3D-Printed Nylon Projectile Geometries With Thickness Accuracy of 0.099 Mm. (B) The Front View Of The Experimental Setup Consists Of A Movable Lab Jack Attached to an Aluminum Frame at the Top And Electromagnet At the Bottom. A Crystallizing Dish Filled With the Granular Target is Placed Right Below the Lab Jack.33

Figure	Page
<b>Figure 12.</b> Comparing Angle Of Repose For Base Method And Arc Tangent Method For Various Particle Size Distributions. ....	36
<b>Figure 13.</b> Conditioned Bulk Density Of Glass Beads, Obtained From FT4 Experiments .....	37
<b>Figure 14.</b> Basic Flowability Energy Of Glass Beads Against Their Particle Size Distribution .....	39
<b>Figure 15.</b> Specific Energy Of Glass Beads With Respect To Their Particle Size Distribution .....	40
<b>Figure 16.</b> A) Linear Fit Plot For Aor Vs BFE B) Linear Fit Plot For Aor Vs SE C) Linear Fit Plot For Aor Vs Cohesion.....	42
<b>Figure 17.</b> A) Linear Fit Plot For CI Vs BFE B) Linear Fit Plot For CI Vs SE C) Linear Fit Plot For HR Vs BFE D) Linear Fit Plot For HR Vs SE.....	43
<b>Figure 18.</b> Coefficient Of Particle Size Plotted Against The Surface Area Mean Diameters. A Linear Regression Line Is Used To Fit The Data To Develop A Relationship Between The Two Factors. The Goodness Of Fit Was Evaluated By $R^2$ Value That Was Found To Be 0.94. ....	45
<b>Figure 19.</b> Torque Values For 250-355 (Green) And 430-600 (Blue) Micron Glass Beads With 0.5% Moisture. The 430 – 600 Micron Particles With Peaks Demonstrate Slippage In Material.....	47

**Figure 20.** Fitted Curves For Shear Cell Data Of Glass Beads For Various Moisture Percentages. The Corresponding Psds Are **A)** 5-11  $\mu\text{m}$  **B)** 25-50  $\mu\text{m}$  **C)** 70-100  $\mu\text{m}$  **D)** 120-180  $\mu\text{m}$  **E)** 180-250  $\mu\text{m}$  **F)** 250-355  $\mu\text{m}$  ..... 51

**Figure 21.** Correlation Between The Experimentally Obtained Values Of The FFC And Those Predicted By The Empirically Developed Model ..... 53

**Figure 22.** Experimental And Theoretical Penetration Depths Of Spherical Projectiles. (Inset) Tabulated Values.  $H$  Represents The Total Release Height, Which Is The Sum Of The Release Height,  $H$ , And The Experimental Penetration Depth,  $D_{\text{exp}}$ .... 55

**Figure 23.** Penetration Depths Of Various Projectile Geometries As A Function Of Release Height. .... 57

**Figure 24.** Comparison Of Theoretical Penetration Depth Values Calculated From Eq. (2) ( $D_{\text{eq.3\_Cylinder}}$ ), Eq. (3) ( $D_{\text{eq.4\_Multi-Shaped}}$ ), And Eq. (4) ( $D_{\text{eq.13\_Proposed}}$ ) With The Respective Experimental Values ( $D_{\text{exp}}$ ), And Error Bars Indicating The Standard Deviation. In The Data Interpreted For  $D_{\text{eq.13\_Proposed}}$ , The Average Values Of  $D$  For All Three Shapes (Cylinder, Cuboid And Triangular Prism) From Each Set Was Chosen For Each Release Height. .... 60

#### Appendix Figure

**Figure A. 1.** Corn Stover And Pine Forest Residue Fines Produced From Hammer Milling..... 74

**Figure A. 2.** Effect Of Varying Particle Size Distribution On Basic Flowability Energy (BFE) Of Pine Forest Residue..... 74

Figure	Page
<b>Figure A. 3.</b> Effect Of Varying Particle Size Distribution On Basic Flowability Energy (BFE) Of Pine Forest Residue.....	75
<b>Figure A. 4.</b> Comparison Among BFE Values Of Biomass Samples And Glass Beads .....	75
<b>Figure A. 5.</b> Particle Size Distribution Analysis Of Corn Stover And Pine Forest Residue Fines Acquired From Hammer Milling (As-Is) .....	76
<b>Figure A. 6.</b> Total Energy (TE) Of Unsorted As-Is, Oven-Dry, And Sieved Biomass Samples. The Test Number On The X-Axis Indicates The Number Of Times TE Is Measured Per Experiment. Before Each Test, The Sample Is Conditioned To Maintain A Homogenous Distribution Of The Material.....	77
<b>Figure A. 7.</b> (A) Basic Flowability Energy (BFE), (B) Specific Energy (SE), And (C) Aerated Energy (AE), For As-Is, Oven-Dried, And Sieved Biomass Samples.....	78
<b>Figure A. 8.</b> Analysis Of Variance For Angle Of Repose Values Obtained From Base Method And Arc Tangent Method.....	79
<b>Figure B. 1.</b> Analysis Of Variance For Penetration Depths Of Various Projectiles In Each Set Used .....	83
<b>Figure B. 2.</b> Fitted Line Plots Of Penetration Depth As A Function Of Length Of The Projectile For All Release Heights Used. ....	85
<b>Figure B. 3.</b> Fitted Line Plots Of Penetration Depth As A Function Of Release Height Of The Projectile For Each Set. ....	86

**Figure B. 4.** Fitted Line Plots Of Penetration Depth As A Function Of Surface Area  
Of The Projectile For All The Release Heights Used..... 87

## CHAPTER 1 INTRODUCTION

Granular materials are defined as a conglomeration of solid, macroscopic, and discrete particles with sizes above 1 micron (Duran & Behringer, 2001). These materials are so ubiquitous in our daily lives that sometimes we can take them for granted. However, these materials are extremely important in the commercial world, as they are profusely used in industries like pharmaceutical, agricultural, mining, food, and cosmetics. Granular materials have complexity in many physical attributes. For example, in an hourglass filled with sand, we can observe how the granular material stays at rest like a solid, flows like a liquid, with particles hitting the base that scatter like gas molecules. Because they behave differently than any standard physical form, they can be considered as an additional state of matter. It is necessary to study these particles' properties, to better understand their diverse behavior and assess their industrial applicability, processing and design.

Particles appear in several shapes, such as spheres, fibers, chips, and elongated cylinders. Particle sizes can vary widely from several centimeters down to less than a few microns. Some materials are highly cohesive, while others are free-flowing. Because of such complexity in their physical properties, there is a lack of correlation of these properties to performance metrics and efficiency of pre-processing operations in industries dealing with various granular materials. During pre-processing operations, feedstock material and environmental parameters like density, particle size distribution, and moisture content can affect the material flowability and consequent material handling, transportation, and storage. This research will focus on studying the effects of such parameters on powder flow



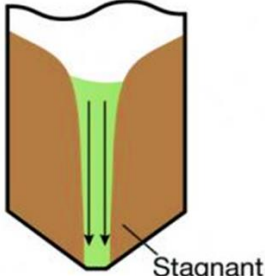
properties alongside developing a model to predict the flow using dynamic flow characterization with a rheometer.

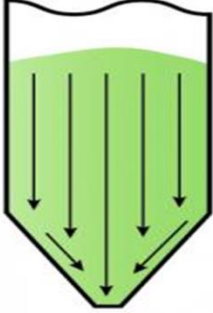
### 1.1. Flowability

In simple terms, flowability is the ability of a material to flow. However, it is not an internal property of a material, nor can it be interpreted as a single value (Prescott & Barnum, 2001). It is a consequence of several other parameters, like the environment, physical properties of the material, and the handling equipment. Therefore, a fitting definition for flowability would be the capability of a material to flow in a desired manner in a specific piece of equipment (Prescott & Barnum, 2001). Flow patterns affect the way a material flows, and can be categorized as funnel flow or mass flow, as described in Table.1.

Table 1

*Types of flow patterns in silos and hoppers* (Mass Flow and Funnel Flow Hoppers, n.d.; Mehos et al., 2018)

Type of flow pattern	Definition	Representation	Advantages	Disadvantages
Funnel Flow	Material at the center discharges faster than the material near the sidewalls		<ul style="list-style-type: none"> <li>• Reduced abrasion of side walls, due to limited movement of material</li> <li>• Offers larger capacity to hold the material with reduced vertical height</li> </ul>	<ul style="list-style-type: none"> <li>• Unpredictable discharge of material</li> <li>• Risk of causing arching, ratholing and flooding</li> </ul>

Mass Flow	First-in, first-out movement of materials		<ul style="list-style-type: none"> <li>• Uniform discharge of material</li> <li>• No arching or flooding</li> </ul>	<ul style="list-style-type: none"> <li>• May require tall geometries, which can hinder optimization of equipment design</li> <li>• Not suitable for all materials</li> </ul>
-----------	---	---	---	--

### 1.2. Common flow issues

Though the mass flow pattern is preferred in most scenarios, it is not always achievable. Design constraints and physical properties of the material can prompt funnel flow and the disadvantages that coincide. Almost every factory that deals with hoppers and silos comes across a downstream issue, where the material refuses to flow. In some cases, this is seen in the form of arching where the powder is blocked at the outlet. In other cases, there is an empty funnel going from the top to the bottom of the silo, with the material stuck to the walls. This is called ratholing. Arching happens when cohesive powders are stored in a hopper that does not have a large enough outlet or steep enough walls. Ratholes usually happen in hoppers that are not designed to be mass flow silos and have too small of outlets.

Both ratholing and arching are related to flowability properties of the bulk material. Determining a critical outlet diameter and a suitable hopper wall angle ensure a good flow without arching or ratholing. These parameters can be determined using shear cell testing and a rheometer. It is therefore crucial to understand different types of flow issues and their root causes to conduct suitable flowability characterization and optimize the design

parameters of hoppers and silos. In **Fig. 1**, a schematic of these issues is summarized.

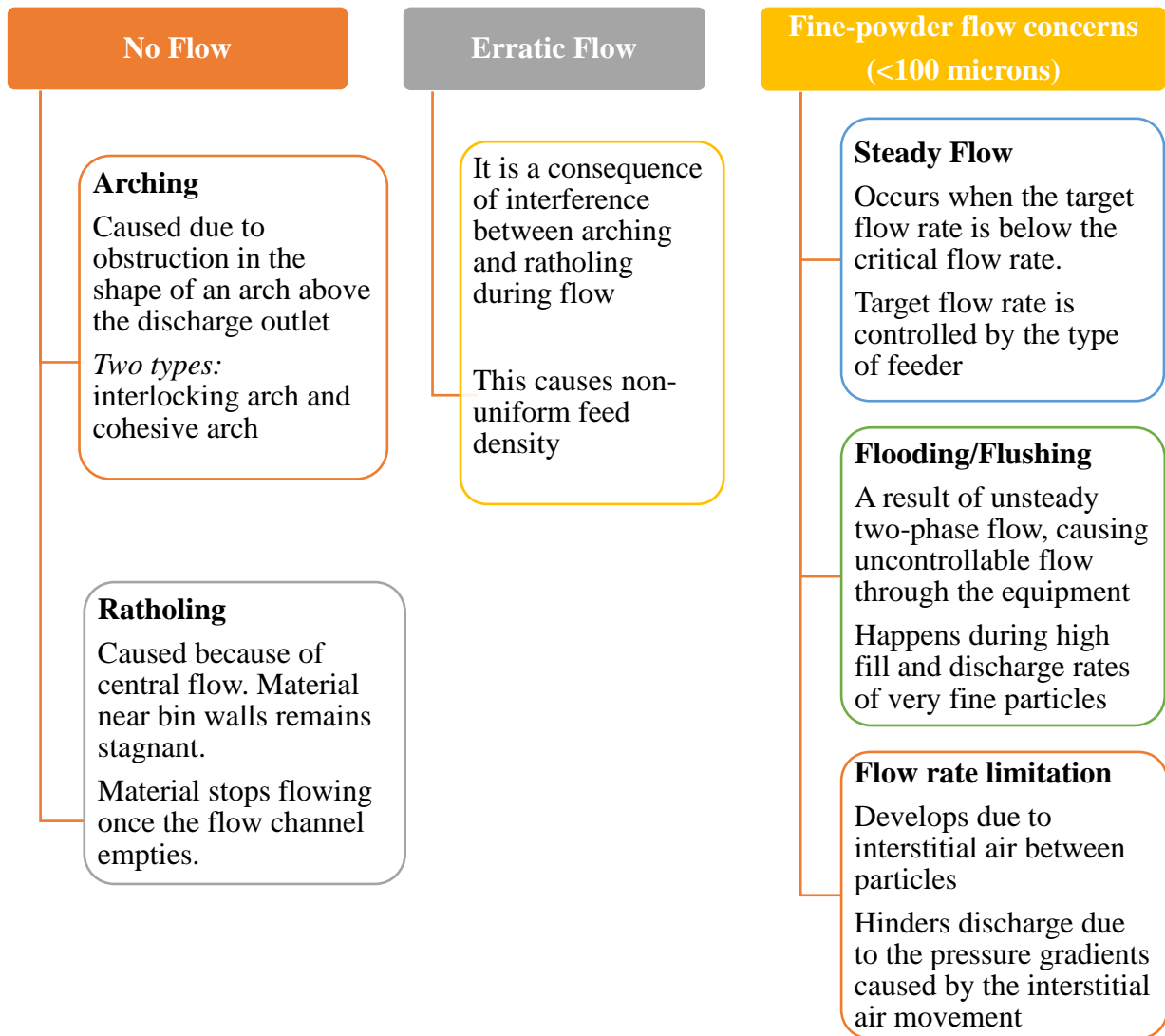


**Figure 1.** Classification of flow issues. (Baxter & Prescott, 2017)

### 1.3. Thesis Objectives

According to the National Fire Protection Association, particles of <420 microns of mean diameter and <25% moisture level are categorized under dust. Fines include a slightly wider range, peaking up to 1 mm mean diameter. These size ranges are generally involved

in processes like pelletization and pneumatic conveying in biorefineries and power plants. Pelletization involves compaction of particles not higher than 3 mm in narrow die channels. They are expected to have high durability of >98% in order to avoid dust explosions and self-ignition. To acquire this standard, it is important to find an optimal particle size range that delivers the right amount of cohesion and stability. On the other hand, refineries and powerplants that carry out operations like pneumatic conveying need an effective method to keep the flow of these particles uniform by using optimal particle sizes. This ensures efficient conveying and safe handling.

In the particle field, there is a lack of substantial knowledge on flowability, interparticle cohesion and their correlation with physical parameters in the finer spectrum of size ranges. Through this work, we aim to study the relation between particle size, moisture and density on flowability of bulk solids that fall under the fines category. To address them, the following objectives are covered in this work:

1. Study the effects of particle size distribution on confined and unconfined flow energy of granular materials.
2. Compare the conventional flowability descriptors of angle of repose, Carr's index and Hausner ratio to flow properties obtained from the FT4 rheometer, and conduct a statistical analysis.
3. Study the shear properties of particles with various particle sizes and moisture levels using a shear cell tester and derive flow function coefficients (FFCs).
4. Develop a model to predict the FFC for a bulk solid with a particular particle size and moisture content.

5. Study the impact of solid projectiles of various geometries on a granular target and derive an empirical relation that can predict the penetration depth of such objects, given the base surface area and release height of the projectiles.

## CHAPTER 2 LITERATURE REVIEW

Recently, several works have focused on studying parameters affecting the flowability of various granular materials and ways to improve the flow, some being experimental (Anderson & Mitchell, 2016; Coombes & Yan, 2015; Crawford et al., 2016; Cui & Grace, 2007; R. E. Freeman et al., 2009; Fu et al., 2012; Hilbert & Solt, 2008; Roberts & Scott, 1992; Saw et al., 2015; Shi et al., 2018; Tannous et al., 2013; Trubetskaya et al., 2017; Viana et al., 2018; Xu et al., 2019), and a few numerical (Chum, 2015; A. Grima et al., 2011; A. P. Grima et al., 2011). A majority of these works relied on conventional methods and parameters such as the angle of repose, Hausner ratio, and shear testers like the Schulze ring shear tester. Presently, the majority of the testing to characterize flow in both industry and academia has been shear testing due to its quality and reproducibility (Shi et al., 2018). A summary of some of the widely used conventional methods to characterize flowability is provided in Table 2, based on the studies carried out in Abdullah & Geldart, 1999; Amidon et al., 2017; Thalberg et al., 2004; and *Uniaxial Powder Tester – Micromeritics*, n.d .

Table 2

***A summary of conventional flowability descriptors for granular materials***

Test method	Technique	Application	Limitations
Bulk density	A sample of known volume is collected in a graduated cylinder and the weight is measured. The ratio of	<ul style="list-style-type: none"> <li>Can provide information on packing of bulk materials.</li> </ul>	<ul style="list-style-type: none"> <li>It is highly dependent on the packing, compaction and</li> </ul>

	<p>mass per volume occupied gives bulk density values.</p> <p>It is important to make sure that the sample is not subjected to any vibrations or tapping while doing this measurement.</p>	<ul style="list-style-type: none"> <li>• It can be used to calculate the Hausner Ratio (<i>HR</i>).</li> </ul>	<p>consolidation of particles.</p>
Tap density	<p>Tap density can be measured similar to bulk density, but in this case the sample is subjected to continuous tapping, until it reaches a maximum packing fraction.</p> <p>The measurement can be performed manually or using a tap density machine.</p>	<ul style="list-style-type: none"> <li>• It acts as an indirect way of indicating changes in structural strength of loosely packed powders and therefore indicate cohesivity and flow characteristics.</li> <li>• It is also one of the parameters in calculating <i>HR</i>.</li> </ul>	<ul style="list-style-type: none"> <li>• The value obtained is dependent on applied compression.</li> </ul>
Angle of repose (AOR)	<p>Obtained by depositing the granular material on a flat surface in the form of a heap through an orifice (cylinders, funnels, hoppers etc.)</p>	<ul style="list-style-type: none"> <li>• It is a straightforward and well-established method that correlates well with the <i>HR</i>.</li> <li>• This method is well suited for materials with low to intermediate cohesion.</li> </ul>	<ul style="list-style-type: none"> <li>• Powders with higher cohesivity do not have a defined AOR.</li> <li>• Results are highly dependent on the measuring technique and are difficult to reproduce.</li> </ul>
Hausner ratio (HR)	$HR = \frac{\rho_{bulk}}{\rho_{tap}}$	<ul style="list-style-type: none"> <li>• It is a useful parameter reflecting particle-particle friction.</li> <li>• A measure of cohesion.</li> </ul>	<ul style="list-style-type: none"> <li>• The main drawback comes from its empiricism.</li> <li>• It is a single index that provides limited information on flowability.</li> </ul>

Carr's Index	$\text{Carr's Index} = \frac{\rho_{tap} - \rho_{bulk}}{\rho_{tap}} \times 100$	<ul style="list-style-type: none"> <li>• An estimation of how material flows based on the assumption that the compressibility is related to flowability</li> </ul>	<ul style="list-style-type: none"> <li>• Similar to HR, this is also an empirical relation and provides limited information on powder flow</li> </ul>
--------------	--	--	---

Although the conventional methods mentioned in Table 2 indicate powder flowability and are relatively cheap and easy to operate, their main limitations arise when dealing with cohesive and complex-shaped materials. For instance, due to the low bulk density, high compressibility and severe entanglement of biomass particles, it is challenging to create a well-defined shear zone and steady-state flow (Xu et al., 2019). Standardizing the correlations between physical attributes and flow properties of granular materials steers efficient handling, storing and processing operations. In addition, when dealing with bulk materials with small particle sizes, fines building up and adhering to the conveying system's inner walls or chute walls is a major issue (Hilbert & Solt, 2008). These are granular materials with very fine particle size that tend to clump together due to their increased surface area and cohesiveness. Both ratholing and arching can be caused due to particle interlocking and increased cohesive strength of the bulk material.

Several methods have been implemented to avoid fines buildup via air cannons (Martin Engineering, n.d.), liners (Mitsubishi Chemical Advanced Materials, n.d.), and equipment design (Cleveland Vibrator Company, 2016; A. P. Grima et al., 2011; Roberts & Scott, 1992). But maximum improvement in flow of such materials is only possible when there is optimization in equipment as well as particle properties.



The literature is lacking a general model relating the basic properties of bulk particulate materials like particle size, particle shape, moisture content, and surface roughness with the bulk powder flowability metrics like the flow function factor, shear strength, and the Hausner ratio. Developing a better understanding of the relationship between these particle parameters and bulk powder flowability can improve our knowledge in designing better bulk material handling equipment, choose better powders for manufacturing, and potentially avoid flowability problems.

### ***2.1. A summary of conventional flowability descriptors***

In the following portion of this section, the studies based on conventional flowability descriptors listed in Table 2 will be summarized, followed by highlighting more reliable and newer methods.

Angle of Repose (AoR) is one of the most common methods that is currently used to understand the flowability of the materials. It is a very versatile process because there are different instruments and methods used to characterize AoR. The general equation used to measure the angle of repose is given by Eq. (1), where  $h$  represents the vertical height of the cone and  $r$  represents the base radius:

$$AOR = \left[ \tan^{-1} \frac{h}{r} \right] \quad (1)$$

Wouters & Geldart (1996) developed their own AoR measuring system which can be used for both cohesive and free-flowing particles. The method involved sodium bicarbonate (31-113  $\mu\text{m}$ ) or sodium carbonate (20-50  $\mu\text{m}$ ) flowing through a conical flask at a 45 degree angle and deposited as a cone on the board placed below the setup. The height ( $h$ ) of the cone and the base radius ( $r$ ) were measured. AoR was calculated using Eq. (1).

Another method that is standard in industry practice and in research is to measure the angle of repose using the arctangent method (Beakawi Al-Hashemi & Baghabra Al-Amoudi, 2018). The procedure followed is similar to the right and left base method, where a line is drawn perpendicular to the horizontal base line up to the highest part of the cone. The vertical line does not need to intersect the middle of the horizontal line. Instead, it should intersect the horizontal line directly below the peak. Using Eqn. (2), the arctangent angle of repose is calculated in degrees:

$$\text{angle(degrees)} = \arctangent\left(\frac{\text{height}}{0.5 * \text{length}}\right) * \frac{180}{\pi} \quad (2)$$

Wang et al. (2010) carried out AoR measurements using pulverized coal (0-150  $\mu\text{m}$ ) with different moisture contents similar to Wouters & Geldart (1996), but with two variations, i.e., the base had either a variable or a fixed length. The sliding method used a rectangular box which was filled with the particles. The box was tilted until the particles began to slide. The AoR in this case was the angle between the upper end of the box and the horizontal. It was also important to note that the angle measured using the sliding method was the greatest when compared to the variable or fixed base length method.

Descriptors based on the compressibility of the bulk solid are also popularly used to quantify flowability. The Hausner ratio is the ratio between the tapped density of a material and its bulk density, while the Carr Index is the ratio of the difference between the bulk and tapped density to the tapped density, times 100. The Carr Index assigns a score to the bulk solid between 0 and 100, with 0 being the worst possible flowability and 100 being the best. The parameter that was chosen for this investigation is called the *Flow Function*

*Coefficient*, or FFC. It is a parameter that can be used to characterize flowability of tested granular materials by using both the unconfined yield strength and the major consolidated stress of a given material. It is the ratio of the consolidation stress to the unconfined yield strength, or cohesive strength, of a bulk solid. It is a dimensionless number that is used to describe the nature of flow of the bulk solid numerically. FFC has positive non-zero values, with increasing FFC values indicating increasing flowability in bulk solids. Table 3 shows the different classifications of the Carr Index, the Hausner Ratio, and the FFC with their flowability descriptions alongside them.

Table 3

***Carr Index, Hausner Ratio, and FFC values to quantitatively describe the nature of bulk materials.***

<b>Carr's Index</b>	<b>Hausner Ratio</b>	<b>Flow Function Coefficient (FFC)</b>	<b>Flowability Description</b>
<10	1.00 – 1.11	10<FFC	Excellent
11-15	1.12 – 1.18	4<FFC<10	Good
16-20	1.19 – 1.25	2<FFC<4	Fair
21-25	1.26 – 1.34		Passable
26-31	1.35 – 1.45	1<FFC<2	Poor
32-37	1.46 – 1.59	FFC<1	Very Poor
>38	>1.60		Very, Very Poor

Majid & Nanda (2017) used a Powder Flow Speed Dependence (PFSD) test to characterize flowability by measuring the speed flow properties of the materials, which is considered important in a production environment. The test is done to measure the resistance of the materials with a controlled flow using different blade speeds that operate into the sample. Three main parameters that can be determined using this study are compaction coefficient, flow stability and cohesion coefficient. As the test speed increases,

the compaction coefficient can increase or decrease, which will determine the flowability of the material. Usually, a flow stability index indicates the type of compaction. When the flow stability index is greater than 1, it indicates a higher compaction coefficient, and less than 1 indicates a lower compaction coefficient.

Jenike's shear cell test is another common type of instrument used for flowability studies. It studies the correlation between shear and normal stresses and yields an important value called the yield locus, which is the maximum shear stress of the powdered material under the given normal stress. Opaliński et al. (2012) investigated the effect of moisture on food samples and found that the moisture content had an increasing effect on the shear stress up to 10% moisture levels and an opposite decreasing effect after 10% moisture. It was also concluded that Jenike's shear cell tester was unsuitable for easily deformable particles at higher moisture content due to its long horizontal shear measurements and the difficulty to measure under steady-state conditions.

An FT4 Rheometer is used to measure powder properties in both static and dynamic conditions. Nan et al. (2017b) used spherical and glass beads and polyethylene to study its flow energy functions. The first step of the procedure is the conditioning step, where the blade rotates clockwise and moves up and down. During this motion, a homogeneous distribution of particles is created. Secondly, the blade moves into the particle bed by slicing through it. The shearing motion of the blade in contact with the powder can be measured as torque and force. Søggaard et al. (2019) used 4 different methodologies, namely shear cell, wall friction test, compression and permeability on pharmaceutical excipients. Zegzulka et al. (2020) studied the flowability of 10 different metal powders across three commonly used shear cell instruments: the Ring Shear Tester RST-01.pc (RST),

Brookfield Powder Flow Tester (PFT) and the FT4 Powder rheometer (FT4). The flow index value was the smallest when measured using the FT4, whereas the RST had the highest value. All of the metal powders were classified as free-flowing according to the RST, and the other two classified almost all of the samples as free-flowing, except for copper and titanium.

As discussed above, there are several ways to measure the flowability of the granular materials, but an effective relationship between each of them is not yet concretely described. Many researchers have used the FT4 to characterize bulk and dynamic properties of various granular materials (Bruni et al., 2007; R. Freeman, 2007; Fu et al., 2012; Gnagne et al., 2017; Hare et al., 2015; Jan et al., 2018; Jin et al., 2018; Koynov et al., 2016; Leturia et al., 2014; Lu et al., 2012, 2018; Mitra et al., 2017; Nan et al., 2017a, 2017b; Rohilla et al., 2018; Saw et al., 2015; Shi et al., 2018; Søggaard et al., 2019; Wilkinson et al., 2017). This setup allows for the characterization of consolidated, conditioned, aerated, and even fluidized powder. Other testers do not have all these capabilities, including bulk characterization, and the consideration of external variables like moisture, aeration and consolidation. Additionally, the automatic conditioning of material before every test in the FT4 provides excellent repeatability.

FFC is a relatively easily available quantifier using the FT4, that is widely used in the industry to describe or rank the flowability of bulk solids. This was also one of the reasons it was chosen as the subject of this investigation. The goal was to develop a model that would be able reliably predict the FFC for a bulk solid with a particular particle size and moisture content, without having to perform experiments every time, resulting in savings in resources and energy.

## ***2.2. Literature review on impact of projectiles on granular media***

Many studies on projectile penetration in granular targets have been published in the last 50 years, examining a variety of process parameters such as target material, geometry and velocity of impacting object, and crater formation. A brief literature survey for the response of granular media to penetration, categorizing the applied methodologies into analytical, computational, and experimental methods, are presented in this section.

The impact mechanism is dependent on parameters like particle size of the target material (Feng et al., 2019), packing fraction (Tapia et al., 2013), penetration depth (Peng et al., 2019), projectile shape (Lobo-Guerrero & Vallejo, 2007) and impact velocity (Nazhat & Airey, 2015). To predict the effect of asteroids striking Earth, the impact dynamics of high-velocity intruders on dry granular beds were examined (Reimold, 1996). By studying low-velocity impacts, the formation mechanisms of craters were estimated (Ambroso et al., 2005; Katsuragi & Durian, 2007; Takita & Sumita, 2013; Uehara et al., 2003). The movement of different terrestrial creatures on granular terrains such as sand, ice and leaf debris were investigated, such that robots can replicate their locomotion on diversified terrains (Li et al., 2013; Marvi et al., 2014; Sharpe et al., 2015; Zhang & Goldman, 2014).

Several studies (Ambroso et al., 2005; Clark et al., 2015; de Bruyn & Walsh, 2004; Goldman & Umbanhowar, 2008; Katsuragi & Durian, 2007; Khan, 2015; Li et al., 2013; Marston et al., 2012; Newhall & Durian, 2003; Nordstrom et al., 2014; Reimold, 1996; Sharpe et al., 2015; Takita & Sumita, 2013; Uehara et al., 2003; Wada et al., 2006; Yan et al., 2013; Zhang & Goldman, 2014) reported experimental and numerical results on the impact of spherical projectiles on both dry and wet granular media. However, very few

researchers (Ambroso et al., 2005; Goldman & Umbanhowar, 2008; Khan, 2015; Newhall & Durian, 2003) focused on the impact of aspherical projectiles on granular media. Different shaped geometries may experience contrasting drag forces upon penetration, resulting in different penetration depths. In almost all impact studies, penetration depth is considered one of the most important quantities of interest, which can be used to determine the drag force experienced by the projectile (Katsuragi & Durian, 2007). Penetration depth is defined as the distance between the original surface and the bottom end of the penetrated impactor (Takita & Sumita, 2013).

For spherical projectiles, Uehara et al. developed a relationship for penetration depth,  $d$ , in dry (non-cohesive) granular targets (Ambroso et al., 2005; Brzinski et al., 2015; Uehara et al., 2003):

$$d = \frac{0.14}{\mu} \left[ \rho_n^{\left(\frac{1}{2}\right)} D^{\frac{2}{3}} H^{\frac{1}{3}} \right] \quad (3)$$

where

$$\mu = \tan\theta_R \quad (3a)$$

$$\rho_n = \rho_s/\rho_t \quad (3b)$$

$$\rho_t = \varphi\rho_g \quad (3c)$$

Here,  $\mu$  is the internal coefficient of friction for the dry granular material,  $\theta_R$  is the angle of repose,  $\rho_s$  is the density of the spherical projectile,  $\rho_t$  is the mass density of the granular target,  $\varphi$  is the volume fraction of the granular target,  $\rho_g$  is the mass density of the granular material,  $D$  is the diameter of the sphere, and  $H$  is the total release height (i.e., the total distance travelled by an intruder, from the point of free fall until it comes to rest after impact) (Brzinski et al., 2015). According to Eq. (3), the penetration depth follows a power

law as a function of total release height, where  $d \sim H^{1/3}$ . For spherical projectiles, the power law is consistent for both shallow and deep penetrations (Newhall & Durian, 2003). However, this equation cannot be used to predict the penetration depth based on a known release height, since  $H$  cannot be determined without prior knowledge of the penetration depth. Another limitation in Eq. (3) is that it is not applicable to non-spherical projectiles.

For non-spherical projectiles, Newhall & Durian (2003) studied the impact of cylindroconical shapes on dry (non-cohesive) loosely-packed granular beds to see how penetration depth scaled with shape parameters. They tested the impact of cylindroconical projectiles of different materials in a vertical orientation with different cone angles and proposed a new equation for the penetration depth that includes the length of the cylindrical projectile, given by (Newhall & Durian, 2003):

$$d = 0.14 \left\{ \left[ \frac{\rho_s L}{\rho_t \mu^2} \right]^{\frac{3}{2}} D_p^{\frac{1}{2}} H \right\}^{\frac{1}{3}} \quad (4)$$

where  $L$  is the length of the cylindroconical projectile and  $D_p$  is its diameter. Interestingly, they concluded that the power law developed for spheres ( $d \sim H^{1/3}$ ) also holds true for cylindroconical shapes (Newhall & Durian, 2003). Eq. (4) was shown to be consistent for deep penetrations, where the penetration depth is greater than the diameter of the projectile, but it deviates from the power law for shallower penetrations. For the cylindroconical shapes, the deeper penetrations are approximately 13 mm or greater. Further work is needed for shallow impacts of non-spherical projectiles, to quantify the penetration depth deviation from the power law.



In addition to Eq. (4), Newhall & Durian (2003) proposed a new equation for the penetration depth of non-spherical projectiles that replaces the term for the projectile diameter with the mass per cross-sectional area and the release height with the velocity:

$$d = 0.11 \left[ \frac{M/A^2}{\rho_i \mu^2} \right]^{\frac{1}{2}} \left( \frac{Av^2}{g} \right)^{\frac{1}{3}} \quad (5)$$

where  $M$  is the mass of the projectile,  $A$  is the cross-sectional area in contact with the granular media, and  $v$  is the impact velocity. Eq. (5) was tested with a real human foot stepped from a release height of 5 cm with a velocity of 100 cm/s, resulting in a penetration depth of 6.7 cm. The results showed to be close to previous experimental observation (Newhall & Durian, 2003). However, there is no further proof or experimental evidence to show whether this equation holds true for a range of projectile shapes and release heights.

With complex shapes, Eq. (3) cannot be used to evaluate the penetration depth, as the only geometrical parameter considered is the sphere's diameter, while other shapes consist of multiple dimensions. Even though Eq. (4) considers the vertical length of the projectile, it still has the diameter of the cylinder as one of the parameters, which restricts the equation's scope to cylinders. Alternatively, while Eq. (5) appears to consider realistic shapes, it is based on a human foot manually stepping on a beach, which can be difficult to reproduce and can have a non-uniform force distribution upon impact.

To address the limitations discussed, in this work, we studied non-spherical geometries with constant density and volume. The effects of base surface area, vertical length and release height were analyzed upon impact and penetration.

## CHAPTER 3 MATERIALS AND METHODOLOGY

### ***3.1. Materials***

Glass beads were selected as the main material of interest in this study. Their uniformity in shape, smooth surface, and availability in several particle size distributions to cover a wide spectrum of cohesive to non-cohesive nature makes them ideal to carry out flowability studies. Particles of varying sizes were obtained from Potters Industries®. These were rated by the manufacturer in the size ranges of 5-11, 25-50, 70-100, 120-180, and 250-350 microns.

### ***3.2. Material preparation***

#### *Antistatic Treatment:*

The first step to preparing the glass beads of a desired size range for both the angle of repose and flowability testing is to prepare the glass beads with an antistatic solution. Even though the dry glass beads are non-cohesive, during transport and storage, they tend to generate static forces, which can make them stick to the walls of test vessels. To eliminate these static bonds, it is necessary to treat them with an antistatic solution. First, the antistatic solution is prepared by mixing 1mL of ASA antistatic spray with 100mL of ethanol in a beaker (Chen et al., 2017). Glass beads are measured out to the necessary volume and placed in a baking pan. The solution is added a few milliliters at a time and then stirred with a spatula until all conglomerates of glass beads are broken up and there is no more antistatic solution to wet the beads. This process is repeated until all of the beads are a consistent darker color from the antistatic solution and appear wet. The beads are allowed to sit overnight and are then used the following day for experiments. Any excess antistatic

solution is stored in sealed containers and labeled. Fig. 2 shows the steps involved in treating the glass beads with antistatic solution.



**Figure 2.** Steps involving antistatic solution treatment

#### *Adding moisture:*

Wet samples were prepared by mixing the different powders with distilled water to make up moisture levels of 0.5%, 1%, 5%, 10%, and 15% by weight. The granular material and water were collected in a Ziplock bag and kneaded together by hand for about 10 minutes, until homogenized before using for the shear-cell testing. It was ensured that the wet specimens were prepared just before the test so that consolidation over time and evaporation were not factors before the start of the test.

### **3.3. Characterization methods**

#### *Angle of Repose (AoR):*

Angle of repose experiments were performed using a funnel and glass beads with antistatic solution prepared as above. The setup can be seen in **Fig. 3**.

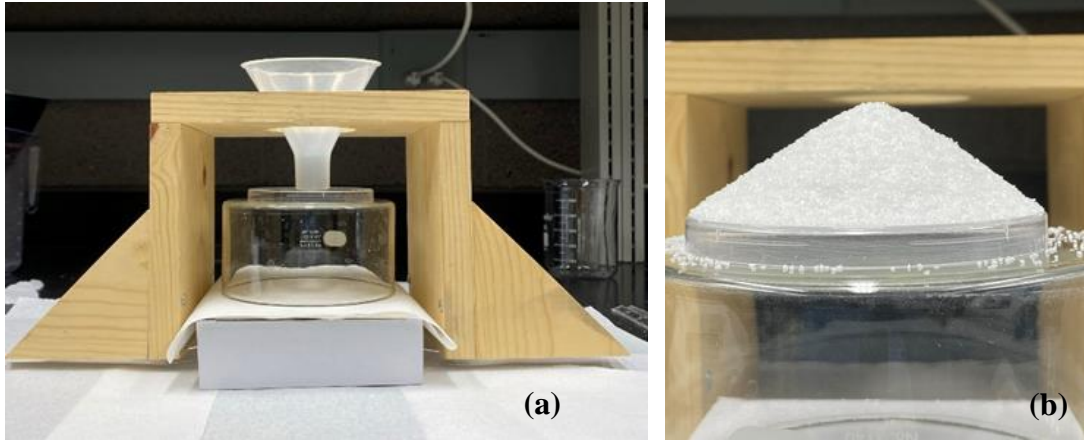


**Figure 3** (a) Angle of repose apparatus; (b) Sample image of the heap formed using the AoR apparatus

A funnel was placed on the stand along with an upside-down crystallizing dish with an inverted petri dish of known diameter (8 cm) on top. The petri dish was held against the base of the funnel to stop particles from descending prematurely. Then the funnel was filled with glass beads. The funnel was gradually lifted so that the particles could flow onto the petri dish until a heap was formed. Additional particles were allowed to overflow on top of the container to measure the maximum angle possible.

A camera was then used to take pictures like that shown in **Figure 3b**, at three different sides. After all trials were completed, the photographs were analyzed using Image J software. In **Fig 4.**, the step by step approach to using an angle tool in Image J is shown. The angle tool was used to find the angle at the base of the cone or through the arctangent method.

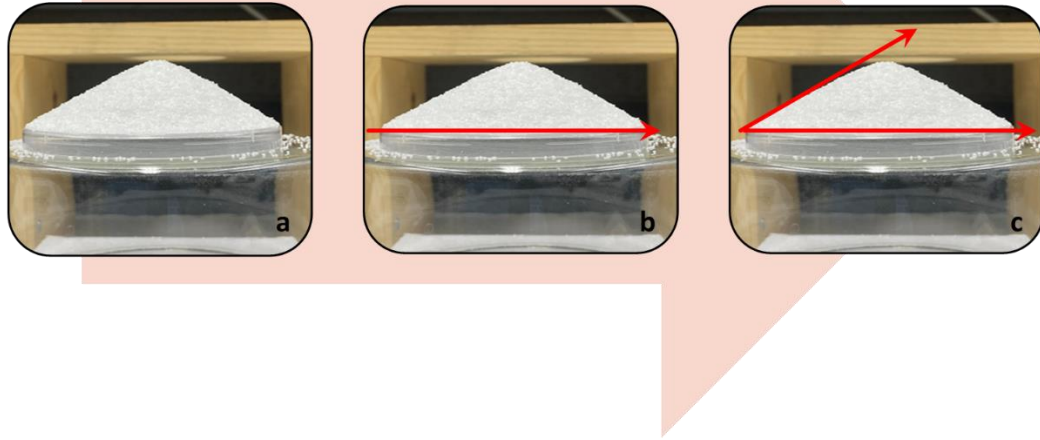


**Figure 4(a).** Sample angle of repose picture; **(b)** & **(c)** Images depicting how the angle tool is used to draw lines in ImageJ

**Fig. 4(b)** shows a horizontal line drawn from left to right using the angle tool, as shown in **Figure 5**. The line was always drawn from the notch on one end of the petri dish to the notch on the other side. Typically, the line was drawn past the end of the petri dish on the side where the angle was being measured. This was so that the angle of the base of the cone could be properly aligned. The line was as straight as possible for the angle of the photo. Next, the other line to create an angle was drawn. It should be drawn to be tangent to the base of the cone. It may take a few adjustments to properly set the line tangent to the base of the cone. When satisfied with the lines drawn, the angle could be read from the menu bar in the ImageJ software (see **Fig. 5**). The angle tool was selected, and the output was the number of pixels in the x and y direction of the drawn angle along with the actual angle.

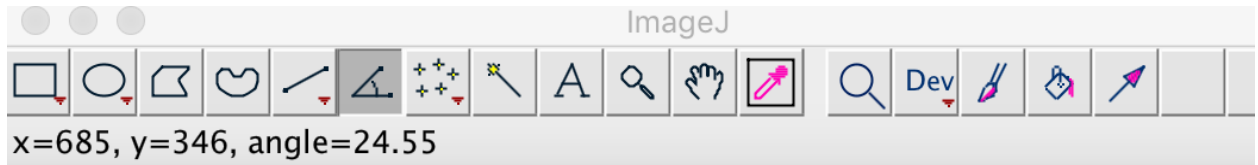


*Figure 5.* ImageJ menu bar with angle tool selected

### **3.4. Particle Characterization**

#### *Particle Size Distribution:*

The size distribution of the particles was measured using the Morphologi G3 (Malvern Instruments Ltd., Malvern, UK). This instrument measures the size, shape, and quantity of particles. The powder sample is loaded into the dispersion unit and is then dispersed onto the observation plate of the instrument. The instrument then proceeds to capture multiple images of the dispersed powder sample. The on-board software then processes these images to calculate particle mean sizes, particle size distributions and various shape factors. The final reported data includes the following size metrics: 10<sup>th</sup> percentile mean diameter, 50<sup>th</sup> percentile mean diameter, 90<sup>th</sup> percentile mean diameter, surface mean diameter – D[3,2], and volume mean diameter – D[4,3]. For the present study, the surface mean diameter - D[3,2] was taken as the principal size parameter for all calculations. It is the surface area mean size of the particle populations, and for the study of flowability effects (that are governed by surface phenomena like surface roughness, adhesion, and cohesion), this parameter was deemed the most appropriate for this application.

#### *Bulk and Tap Density measurements:*

Bulk and tapped density measurement experiments were performed on the dry bulk solid specimens adhering to US Pharmacopeia standard: <616> *Bulk Density and Tapped*

*Density of Powders* (USPC, 2014). The dry sample was gently poured into a 250 ml graduated cylinder and was carefully levelled, avoiding compacting the powder. The uncompacted powder level was then recorded ( $V_0$ ) to the nearest graduated unit. The mass ( $m$ ) of the sample was recorded and the bulk density was calculated by taking the ratio of the mass to the uncompacted powder volume ( $V_0$ ),  $\frac{m}{V_0}$ . Then, the cylinder was secured onto the Sotax TD1 and 10, 500, 1250 taps were performed on the sample and the corresponding volumes  $V_{10}$ ,  $V_{50}$ , and  $V_{1250}$  were recorded. The difference between  $V_{50}$  and  $V_{1250}$  was evaluated. If found to be less than or equal to 2%, then  $V_{1250}$  was taken as the tapped volume,  $V_F$ . If not, the sample was tapped further in increments of 1250 taps until a difference in volume of 2% was observed. The tapped density was then calculated as  $\frac{m}{V_F}$ . The tapped density was measured thrice, and the average of the values was used for the calculation of the Carr Index and the Hausner Ratio.

### ***3.5. Flowability experiments***

After the glass beads were put through initial characterization and preparation, all the chosen particle size distributions were collected into a suitable test vessel, depending on the type of flowability test. Following the test procedures of the rheometer, the experiments were performed. Each range was tested 3 times and each trial had separate containers to maintain the mixing proportions as much as possible. Glass beads were never reused for subsequent rheometer measurements due to a potential change in surface roughness from the blade. A list of quantities evaluated from the flowability experiments are briefly discussed.

#### *Conditioned bulk density*

In simple terms, density defines the relationship between mass and volume of the target material. However, it can vary with slight changes in experimental conditions. Therefore, it must be ensured that the packing of the powder is reproducible. The FT4 has the capability of measuring this value through a conditioning cycle. The consequent value achieved is called conditioned bulk density (BD):

$$BD = \frac{\text{Split mass after conditioning}}{\text{Sample volume}} \quad (6)$$

### *Compressibility*

This quantity is expressed as percentage change in the volume of a given sample for a given applied normal stress. Particle size distribution, cohesivity, particle shape and stiffness, and particle surface roughness are some of the factors that influence this property. It is also expressed as compressibility index, as a function of applied normal stress.

$$\text{Compressed Bulk Density (CBD)} = \frac{\text{Split mass}}{\text{Volume after compression}} \quad (7)$$

$$\text{Compressibility Index (CI)} = \frac{\text{Compressed Bulk Density}}{\text{CBD}} \quad (8)$$

### *Total Flow Energy (TE)*

**Fig. 6** outlines the principle behind measuring the Total flow Energy (TE) using an impeller that rotates and translates upward and downward to create a flow pattern in the particle bed. As the blade is rotating and translating, the FT4 records the corresponding torque and force, respectively, on the blade due to the resistance of the powder to flow.



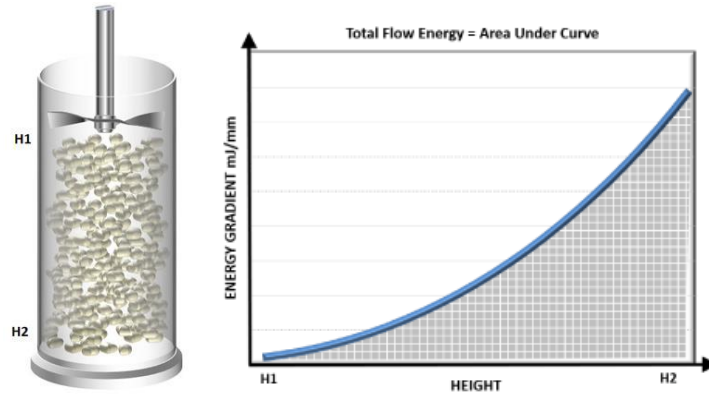


**Figure 6.** A schematic of impeller inside the powder column in the FT4 rheometer. Work done by the blade for each millimeter travelled in the entire column is calculated by the instrument using force and torque values, and an energy gradient is determined. Consequently, the TE is represented by the area under the energy gradient curve (right). The image on the left shows the total distance travelled by the impeller through the powder column from H1 to H2. (*FT4 Powder Rheometer - Dynamic Methodology*, n.d.)

While the TE measurement allows us to interpret the amount of energy required to get the material to flow, it also provides information about the flowability of the material in confined and unconfined situations.

#### *Basic Flowability Energy (BFE)*

The confined flow is measured in terms of the Basic Flowability Energy (BFE) when the impeller is travelling in the downward direction through the powder column. In this case, the powder flow is restrained by the closed bottom end of the test vessel. Confined flow is often found in molding operations and during pelletization (R. Freeman, 2008).

#### *Specific Energy (SE)*

Unconfined flow is measured in terms of the Specific Energy (SE), during the upward movement of the blade. Here, the powder is free to move and is not restricted by a closed top, and flow is induced only through gravitational forces. Unconfined flow often occurs

in industrial processes such as pneumatic conveying and hopper discharge (R. Freeman, 2008).

### *Shear cell testing*

Test specimens for the shear cell testing were prepared by mixing the different powders with distilled water to create moisture levels of 0.5%, 1%, 5%, 10%, and 15% by weight. An upper limit of 15% moisture content was chosen because it was observed from previous studies that above this threshold, the bulk solid transforms into a different flow regime altogether, and it was not deemed practical to try to describe that regime with the same empirical model. Similarly, dry powders were also excluded from the study, as it was observed that they displayed behavior akin to a different flow regime.

The specimen was then poured into the vessel of the rheometer. The FT4 utilizes ‘Test Programs’ to perform each experiment which run independently of the operator, other than the change of the various attachments for different parts of the test. It is a sequence of steps that the instrument takes during a test, which can also be altered to suit a particular use case. A custom test program was run for the wet test specimens adhering to ASTM D7891-15 standards, except that the initial conditioning sequence was omitted as it would trigger a ‘blade height’ error as the cohesive material would stick to the outer edges of the vessel and lead the system to believe that the blade was still immersed in the bulk material.

The sequence of steps that were performed during a test are as follows:

1. The piston was used to compress the test material to a consolidating stress of 9 kPa, following which the vessel was split to remove excess powder by means of a levelling mechanism where the upper half of the vessel splits to expose a flat cross-

section of the consolidated material. The shear cell test was performed on this cross section in the steps that followed (See **Fig. 7**).

2. The vented piston was then swapped with the shear cell. Before the actual shear stress testing began, a series of pre-shear sequences were performed. The consolidating stress was re-established with the shear cell and the material was pre-sheared until a steady state was reached. This process was repeated until two consecutive pre-shears were found to be within 97% of each other in value.
3. The shear stress testing then began with an initial normal stress of 9 kPa. Shear stress was applied to the test specimen until the point of incipient flow (shear test point) was reached.
4. This cycle of shearing until incipient flow was repeated for normal stresses of 7 kPa, 6 kPa, 5 kPa, 4 kPa, and 3 kPa as shown in **Fig 8**.



**Figure 7.** The vessel used for the shear cell test on the FT4. The splitting mechanism is used to get rid of the excess material, resulting in and we are left with a flat surface for the experiment.

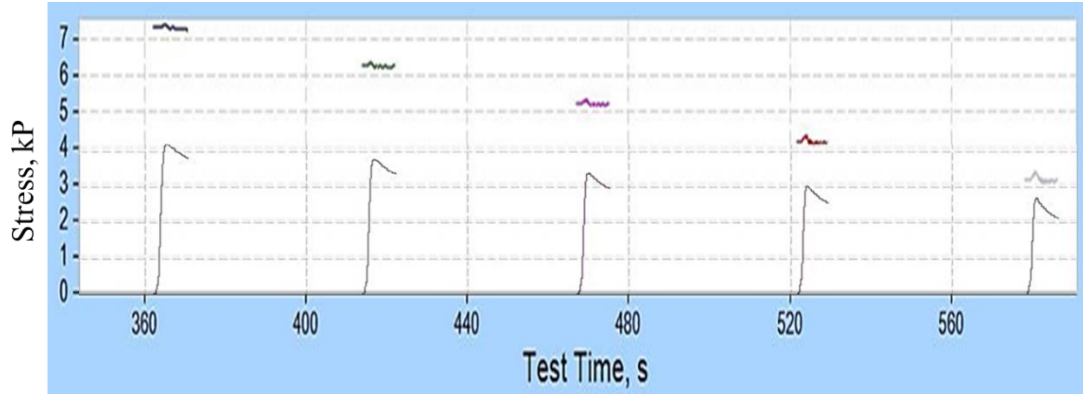


**Figure 8.** Successive shearing operations done in a single shear cell test experiment. The bottom curves are the shear stress plots, with peaks representing the point of incipient flow (shear test points) corresponding to each normal stress value plotted on top.

The shear test points were plotted against their respective applied normal stress. A linear regression line was drawn through these data points to meet the y-axis. This line is known as the yield locus. A Mohr's stress circle was drawn with its center on the x-axis, and tangential to the yield locus (see **Fig 9**). The non-zero intercept of this circle gives the unconfined yield strength,  $\sigma_c$ , of the sample under consideration. A second Mohr's circle is drawn passing through the pre-shear point and tangential to the yield locus. This gives two intercepts, the larger of which gives the major principal stress,  $\sigma_1$ . The ratio of the major principal stress to the unconfined yield strength gives the flow function coefficient (FFC) for each test specimen.

$$FFC = \frac{\sigma_1}{\sigma_c} \quad (9)$$

A flow function value below 4 denotes poor (cohesive) flow, a value between 4 and 10 indicates easy flow, and a value greater than 10 indicates a free-flowing material.

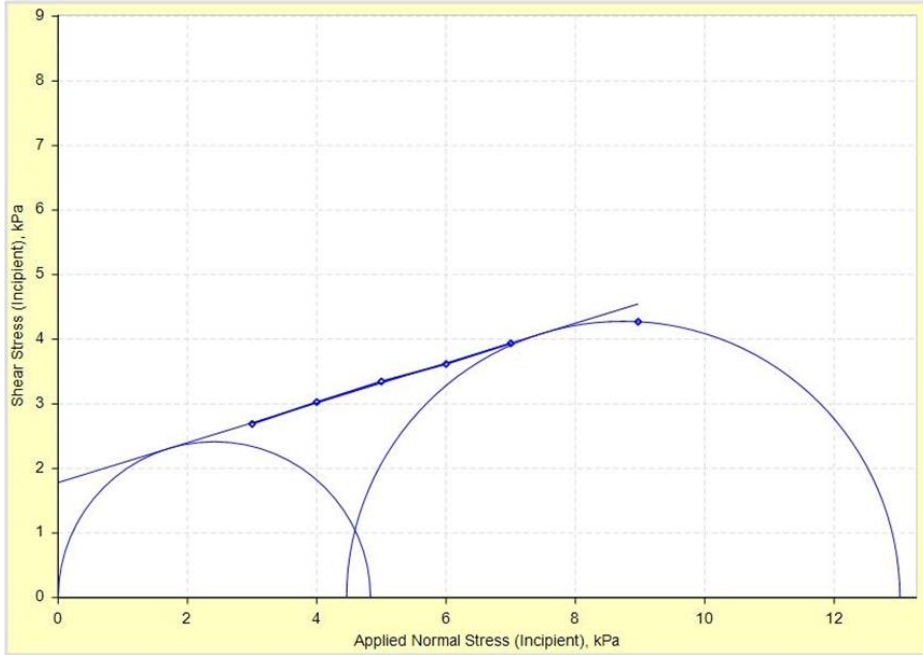


**Figure 9.** The construction of yield locus and the Mohr's circles. The values obtained from the intercepts of the circles are used to calculate the flow function coefficient

**Figs. 10 (a) – (e)** are images of glass beads of  $D [3,2] = 309.9 \mu\text{m}$  at different moisture percentages obtained from the Malvern Morphologi G3. The glass beads can be described to be existing in three distinct states, depending on their intensity of liquid saturation. The glass beads at 0.5%, 1%, and 5% moisture content, **Fig. 10 (a) – (c)**, displayed short and narrow bridges forming between the beads. This state is called the *pendular state*. The beads in these cases are held together by the bonding forces developed due to the liquid bridges. As the liquid content increases, the mixture changes to a *funicular state*, as can be seen in **Fig. 10 (d)**, which shows the glass beads at 10% moisture content. Along with the liquid bridges increasing in volume considerably, the voids in between the beads also start filling up. The beads are acted upon by the bonding force of the liquid bridges along with

the pressure deficiencies introduced due to the surface tension of the water. On further increasing the moisture percentage to 15% (**Fig. 10 (e)**), the mixture transitioned into the *capillary state*, where the capillary forces come into full effect and hold the bulk solid together.

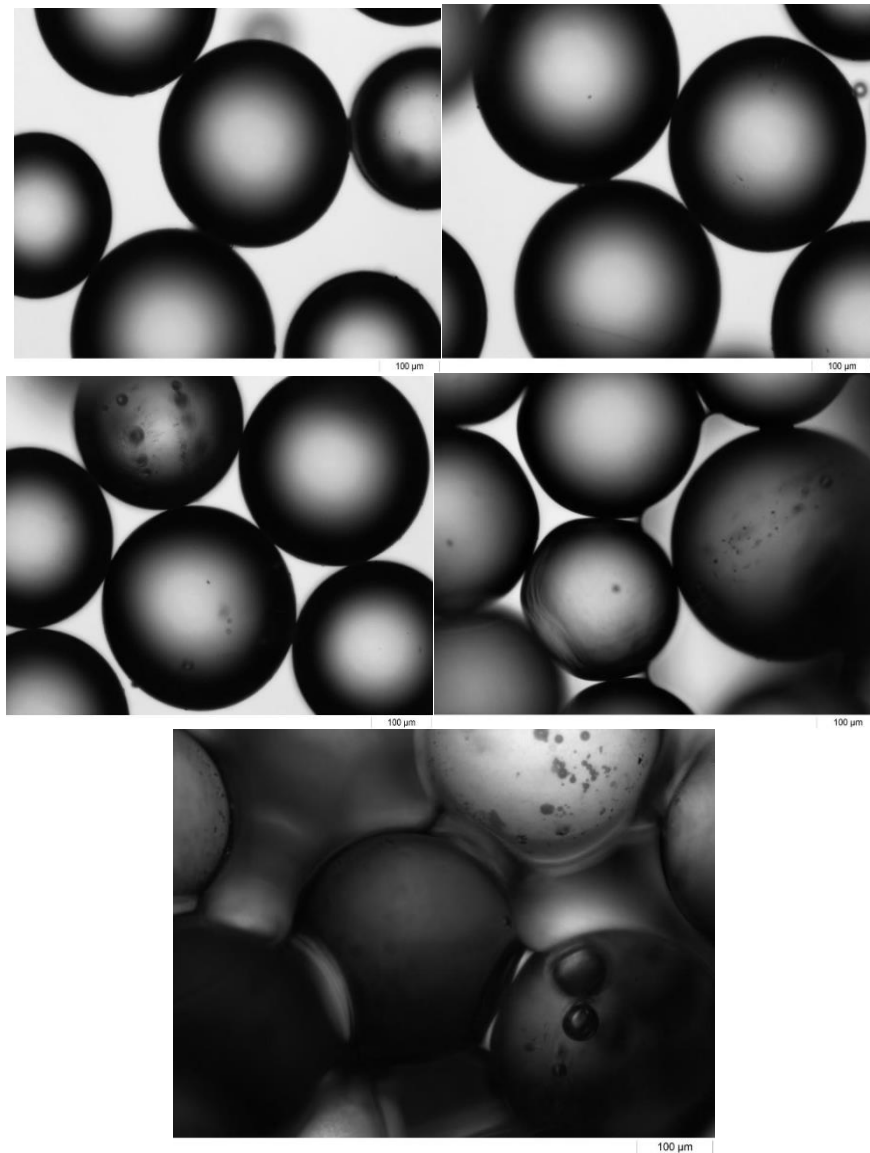


**Figure 10.** (a) 309.90  $\mu\text{m}$  particle size, 0.5% moisture content. Displaying the pendular state. Liquid bridges can be seen forming between the glass beads. The bonding energy from the liquid bridges keeps the beads together. (b) 309.90  $\mu\text{m}$  particle size, 1% moisture content. Displaying the pendular state. (c) 309.9  $\mu\text{m}$  particle size, 5% moisture content. Displaying the pendular state. Volume of liquid bridges increasing further. As the volume increases, the bonding strength

increases, and the beads are packed closer. *(d)* 309.9  $\mu\text{m}$  particle size, 10% moisture content. Displaying the funicular state. Due to the increasing volume content, the liquid bridges start filling up the void in between the glass beads. The surface tension starts playing a part in keeping the beads together. *(e)* 309.9  $\mu\text{m}$  particle size, 15% moisture content. Mixture transitioned into capillary state. The bonding strength between the glass beads is now affected by the capillary pressure of the liquid content of the bulk solid.

### ***3.6. Impact experiments - Methodology:***

Five different projectile geometries were designed: triangular prism, hexagonal prism, cylinder, cuboid, and sphere (see **Fig. 11a**). The geometries were printed with a thickness accuracy of 0.099 mm through a laser sintering technique (EOS Forminga P110 printer) with Nylon 12 as the base material. All projectile shapes had equal base surface areas, while the total volume of each projectile was kept constant (see Table 4). Therefore, theoretically, the masses and densities of all fabricated geometries should also be equal; this was confirmed by weighing each projectile geometry. With the 3D-printed material being non-magnetic, a metal washer was adhered to the base area of the projectiles using an adhesive pad. A mounted suspended electromagnet jack system was used to drop the projectile (see **Fig. 11b**). In the presence of a supplied electric current, an electromagnetic field is produced; in its absence, the projectile falls. By adjusting the lab jack, the projectiles could be dropped from release heights,  $h$ , of 40, 55, 70, 85 and 100 mm into a dry non-cohesive granular media bed.

Silicone glass spheres, supplied by Potters Industries, LLC, with a particle size range of 0.8 - 1.0 mm, were used as the target bed material. The impact experiments were conducted at each desired release height for all projectiles (three replicates of each) prior to adjusting the jack to another desired height. Prior to each trial, the beads were treated

with an anti-static solution to eliminate any charge accumulated on the particles. To avoid the wall effects during impact (Seguin et al., 2008), the container with target material was chosen to be at least eight times the diameter of largest projectile. Furthermore, per each trial, the granular target bed was weighed and the granular media height was measured to ensure a constant packing fraction of 0.602. The impacts were captured using a high-speed camera (FastCam Mini UX100) at 250 fps. The camera's height was fixed at eye level with respect to the granular surface, to avoid parallax error. Once the projectile came to rest after impact, three images were captured in three different viewing angles. The length of the projectile remaining above the granular surface was measured using ImageJ at three different spots on each image, and the penetration depth was calculated using the vertical length values. Only trials in which projectiles remained vertical after impact were analyzed, taking the average of three replicates.

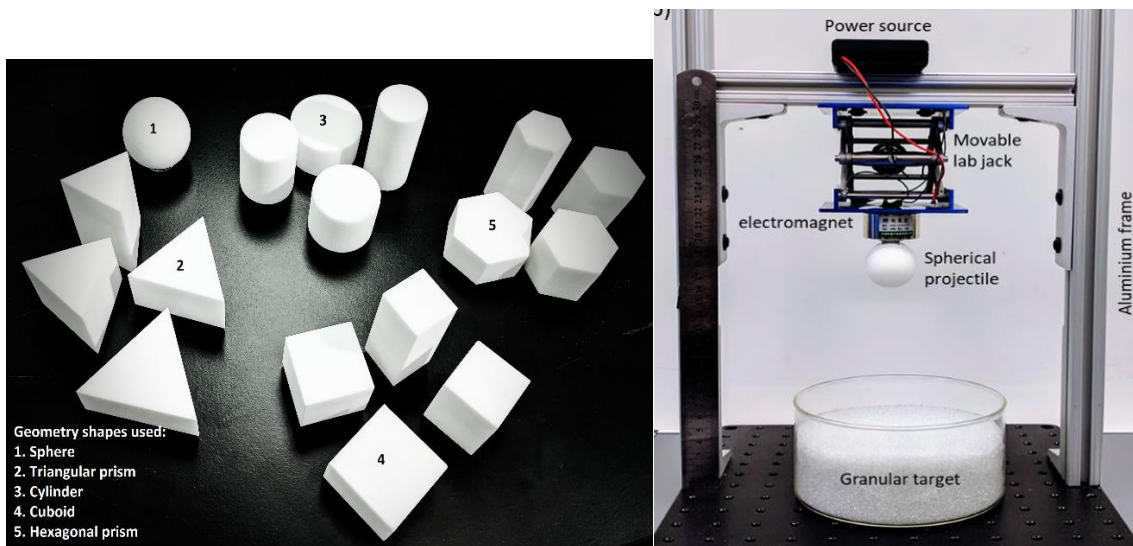


**Figure 11(a)** 3D-printed Nylon projectile geometries with thickness accuracy of 0.099 mm. (b) The front view of the experimental setup consists of a movable lab jack attached to an aluminum frame at the top and electromagnet at the bottom. A crystallizing dish filled with the granular target is placed right below the lab jack.



Table 4

*Experimental parameters, including geometrical and physical properties of the projectiles and the granular target.  $l$  and  $A$  represent vertical height and cross-sectional area of the shapes, respectively.*

Experimental Parameters				
Granular target		Projectile		
Material	Glass beads	Set	$l(\text{cm})$	$A (\text{cm}^2)$
Particle size	0.8 – 1.0 mm	A	5.09	4.91
Mass	1330 g	B	3.53	7.07
		C	2.60	9.62
Bed diameter	320 mm	D	1.99	12.57
Packing fraction	0.602	Volume = 25 cm <sup>3</sup> Mass = 27.2 g Material = Nylon 12 Density = 0.93 g/ cm <sup>3</sup>		
Bulk density	1.50 g/ cm <sup>3</sup>			
Particle density	2.5 g/ cm <sup>3</sup>			

## CHAPTER 4 EFFECT OF PARTICLE AND ENVIRONMENTAL VARIABLES ON RHEOLOGY OF GRANULAR MATERIALS

This chapter covers the outcomes of flowability studies carried out on dry and wet glass beads. The conventional flow descriptors are compared with each other and with the confined and unconfined flow energies of glass beads. The effect of particle size distribution and moisture on flowability and shear properties of glass beads are discussed.

### *4.1. Angle of Repose*

The angle of repose values in **Fig. 12** show a trend where initially there is a decrease followed by an increasing trend as a function of particle size distribution. A lower angle of repose indicates better flow compared to the ones demonstrating higher AoR values. According to the observed values, finer particles had higher AoR, indicating their cohesive nature. With an increase in particle size, the AoR again increased. This could be due to an increase in surface roughness, resulting in higher particle-particle friction, which does not allow glass beads to slide easily. But overall, all of the angles reported were under 30 degrees, which indicate excellent flowability. Therefore, of all the conventional flow descriptors observed, AoR was the most arbitrary.

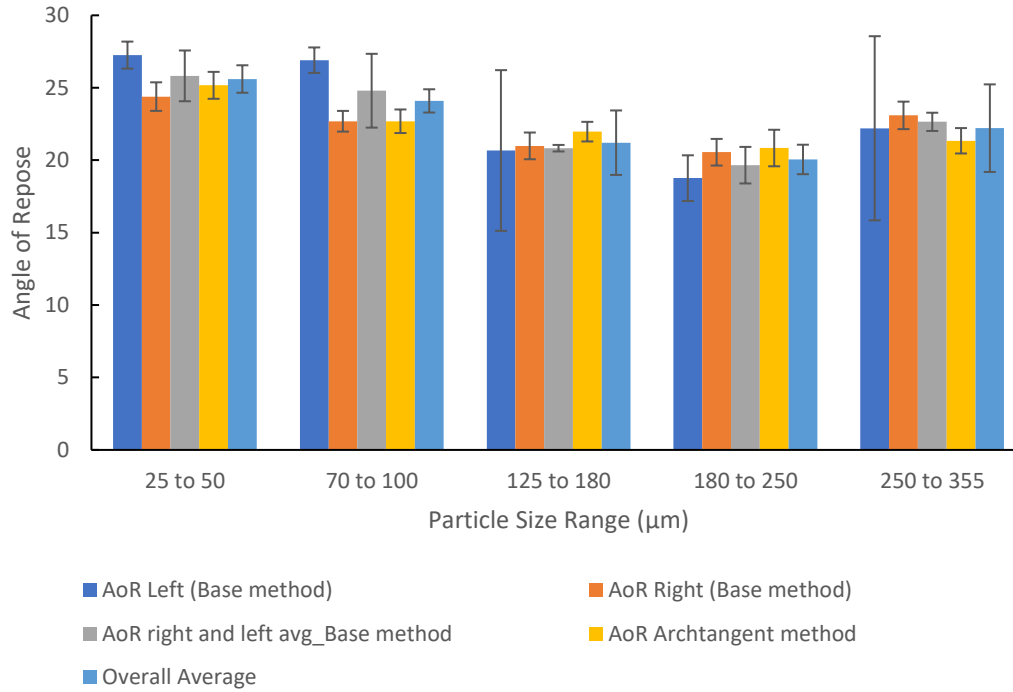


**Figure 12.** Comparing angle of repose for the base method and the arc tangent method for various particle size distributions.

Another important observation while studying the average left and average right values of AoR of the base cone method, and the average of the arc tan method is that their means are equal. This is proved using the One-Way ANOVA, where the P value (0.219) is greater than the significant level (0.05). See **Fig. A.8** for raw statistics.

**4.2. Conditioned Bulk Density (BD):**

The conditioned bulk density values for each particle size distribution are plotted in **Fig. 13**. Except for the size 5-11 microns, all other sizes demonstrated consistent BD values of around 1.5 g/cc with little to no variation, irrespective of their PSD. The standard deviation is indicated in the error bars.

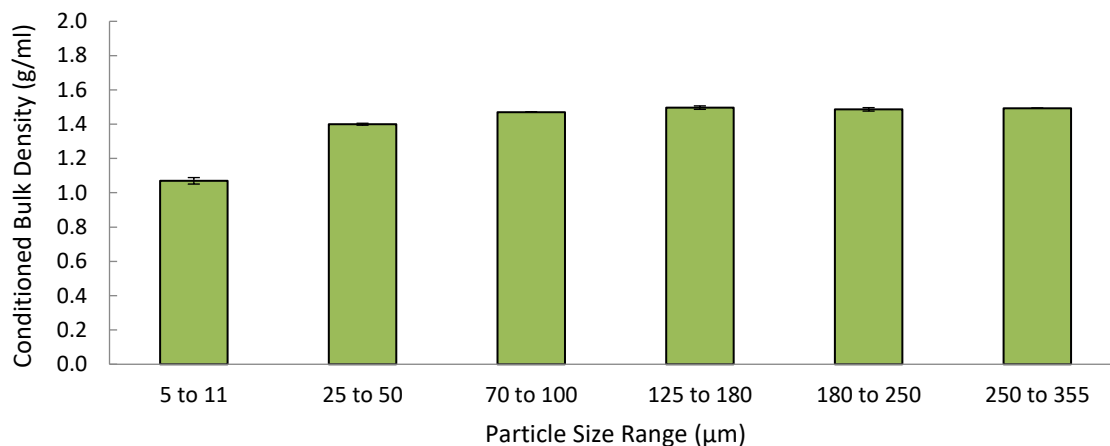


**Figure 13.** Conditioned bulk density of glass beads, obtained from FT4 experiments

### 4.3. Compressibility measurements

The results from the tapped density measurements, averaged over 3 experimental runs, done on dry silica beads, are shown in Table 5. Calculated values of Carr's Index and Hausner Ratio are also presented. This provides an idea of the compressibility of the initial material used for the study.

Table 5

#### *Density-based flowability descriptors of the materials used in the study*

Size range (µm)	Tapped Density (g/ml)	Initial Density (g/ml)	Carr's Index	Hausner Ratio	Flowability Description
5-11	1.44 ± 0.05	0.87 ± 0.04	40	1.67	No Flow
25-50	1.53 ± 0.06	1.31 ± 0.06	14.3	1.17	Good
70-100	1.57 ± 0.07	1.42 ± 0.07	9.5	1.11	Excellent
120-180	1.57 ± 0.05	1.47 ± 0.05	6.4	1.07	Excellent
180-250	1.56 ± 0.07	1.48 ± 0.06	5	1.05	Excellent
250-355	1.57 ± 0.07	1.49 ± 0.07	5	1.05	Excellent

As can be seen from Table 5, the glass beads with particles in the size range of 5-11  $\mu\text{m}$  show the highest values of Carr's Index and Hausner Ratio, indicating very high compressibility. For 25- 50  $\mu\text{m}$ , both bulk density and tap density increased slightly, suggesting a relatively lower compressibility and cohesivity. For sizes starting from 70 – 100 microns the tap density did not vary a lot. This indicated a reduction in compressibility of the material and implied that the cohesivity reduced. But there is still a small hike in bulk density values. On the other end of the spectrum, the materials in the 250-355  $\mu\text{m}$  size range have the lowest value of Carr's Index and Hausner Ratio, indicating the lowest compressibility. These particles are also the most free-flowing, as low values of Carr's Index and Hausner Ratio correspond to better flowability. Though from the values in Table 5, it can be said that all bulk materials in the study with particle size greater than 70 microns have excellent flowability, the materials can be listed as: 250-355  $\mu\text{m}$  > 180-250  $\mu\text{m}$  > 120-180  $\mu\text{m}$  > 70-100  $\mu\text{m}$  > 25-50  $\mu\text{m}$  > 5-11  $\mu\text{m}$  in decreasing order of their ease of flow. Both CI and HR did a good job in differentiating the flowability of these size ranges by highlighting the regime in which these materials come under. However, neither of them provided information about whether these flow regimes were applicable in both confined and unconfined environments.

#### ***4.4. Basic Flowability Energy (BFE)***

**Fig. 14** demonstrates the BFE values, which correspond to the confined flow of material. Although the 5-11 micron beads were highly cohesive, the low BFE value implies good flow, which is not true. This suggests that the low BFE does not necessarily indicate the free-flow regime for every scenario. In this particular case, the impeller rotating through the sample made a hollow column in the center. This is caused by

cohesive particles which refuse to come back to their original position after the impeller pushes them away. Contrary to this, with an increase in particle size, initially the BFE has decreased. This signified that in confined conditions, cohesivity played a key role in controlling the flowability of materials. For finer sizes, due to higher cohesivity, the energy required to initiate flow was higher. However, it was also observed that the BFE values again gradually increased with an increase in particle size, though they are non-cohesive. This indicated that the particles with larger sizes may not flow well in confined situations. This could be due to a higher number of inter-particle collisions and lesser scope for the particles to rearrange themselves due to limited mobility.

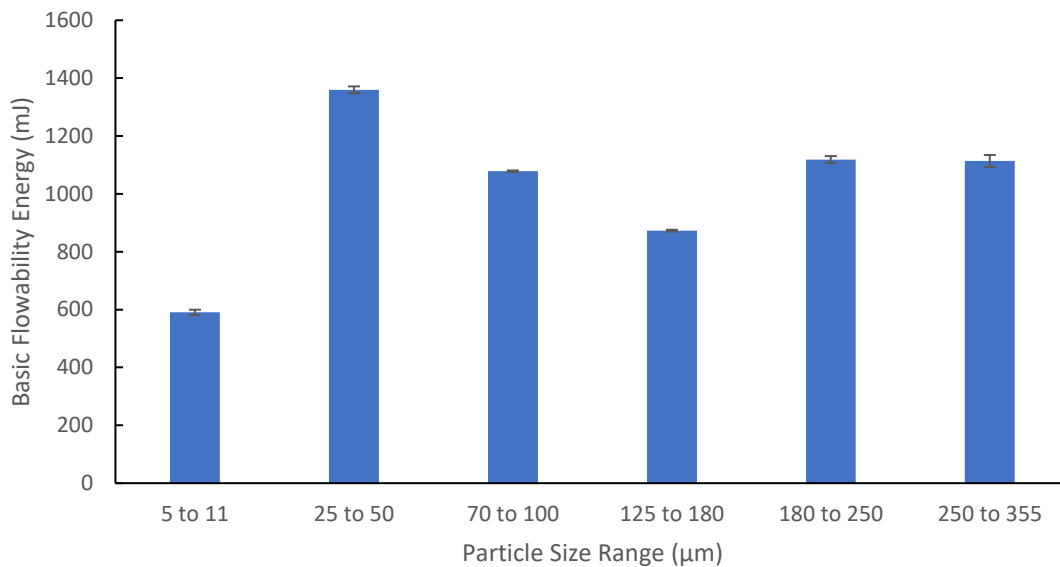


**Figure 14.** Basic flowability energy of glass beads against their particle size distribution

#### **4.5. Specific Energy (SE)**

Specific energy represents the unconfined flow conditions. SE of various glass beads was plotted against their particle size distribution in **Fig. 15**. This followed a similar trend to BFE, except for the finest particles in the sample set which is 5-11 micron size range. This size range exhibited a high specific energy value indicating a poor flow regime in unconfined flow environments. As particle size increased, there was a drop in SE until 125-180 microns, and it increased again for the 180 – 350 microns size range. After 180-250 microns, the unconfined flow energy did not vary a lot.

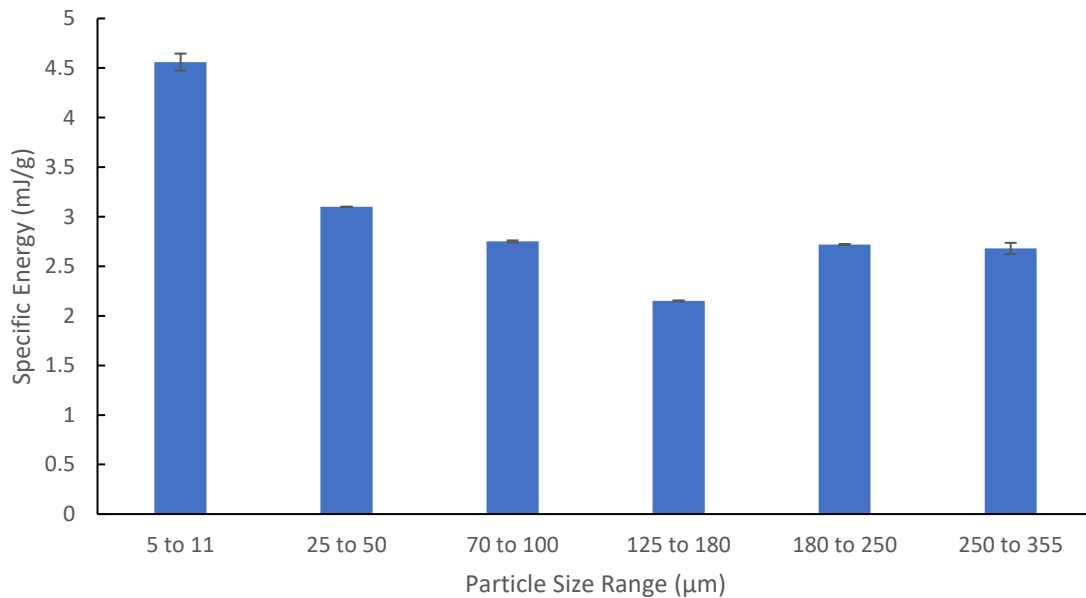


**Figure 15.** Specific energy of glass beads with respect to their particle size distribution

A linear regression analysis was carried out on individual parameters to examine how well the AoR, CI and HR indicate flow properties by comparing them to the BFE and SE values. The following observations were made.

The bulk density of the material remained constant, irrespective of its particle size range, CI, HR, BFE and SE. As the cohesivity increased, the angle of repose became highly unpredictable with no definite trend. **Fig. 16** presents the regression plots for angle of repose vs BFE, SE and cohesivity, to show that the fit was arbitrary. The  $R^2$  values were 31.8, 23.1 and 12.7% respectively. The P-values were calculated to confirm the statistical significance for a significance level of  $\alpha = 0.05$ . For AoR vs BFE, the P-value was 0.19 and for AoR vs SE, it was 0.27, while the P-value for AoR vs cohesivity was 0.35. Since all of the P-values were greater than  $\alpha$ , there was no significant association between these quantities. From this, we concluded that AoR cannot indicate accurate flow conditions in both confined and unconfined environments, as well as for cohesive materials.



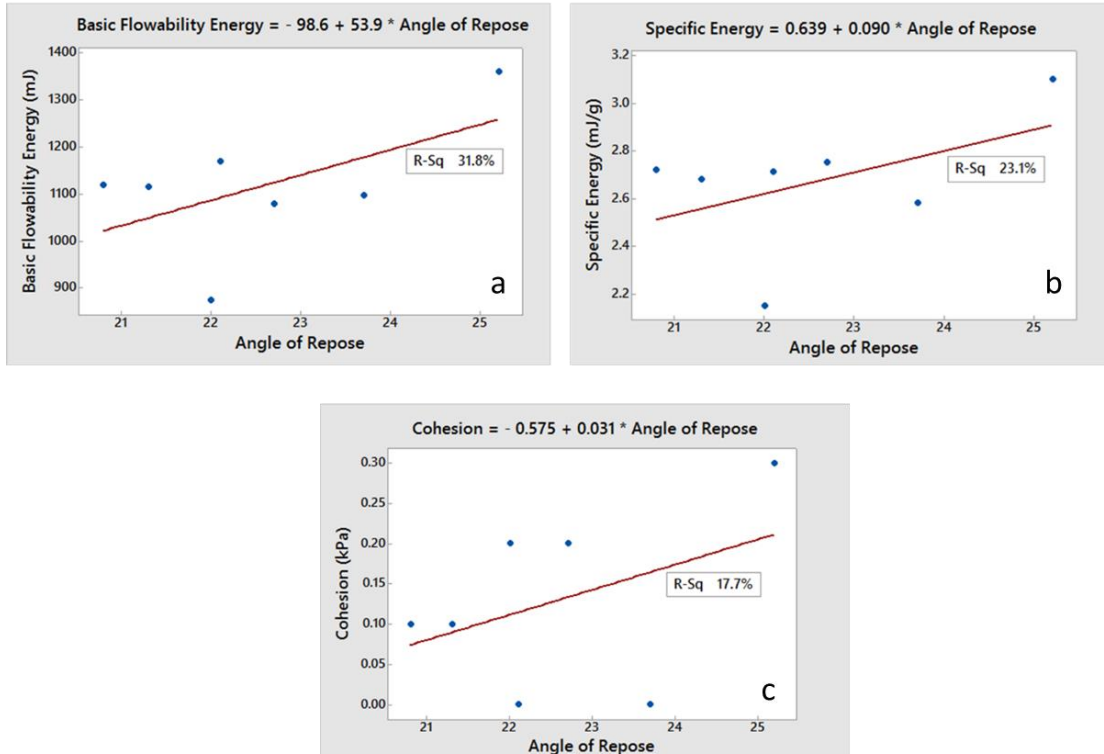


**Figure 16.** a) Linear fit plot for AoR vs BFE b) Linear fit plot for AoR vs SE c) Linear fit plot for AoR vs cohesion

Next, we plotted the Carr's Index and Hausner ratio against BFE and SE (see **Fig. 17 (a)-(d)**). It was interesting to note that both the Carr's Index and Hausner ratio showed a good fit with SE ( $R^2=92.1\%$  for CI and  $91.6\%$  for HR), but not the BFE ( $R^2=45.4\%$  for CI and  $51.5\%$  for HR). With an increase in CI or HR, SE increased, which means that as the flowability of a material decreases, the energy required to initiate flow in unconfined environments also increased. However, for confined flow, neither CI nor HR could predict a definite pattern.

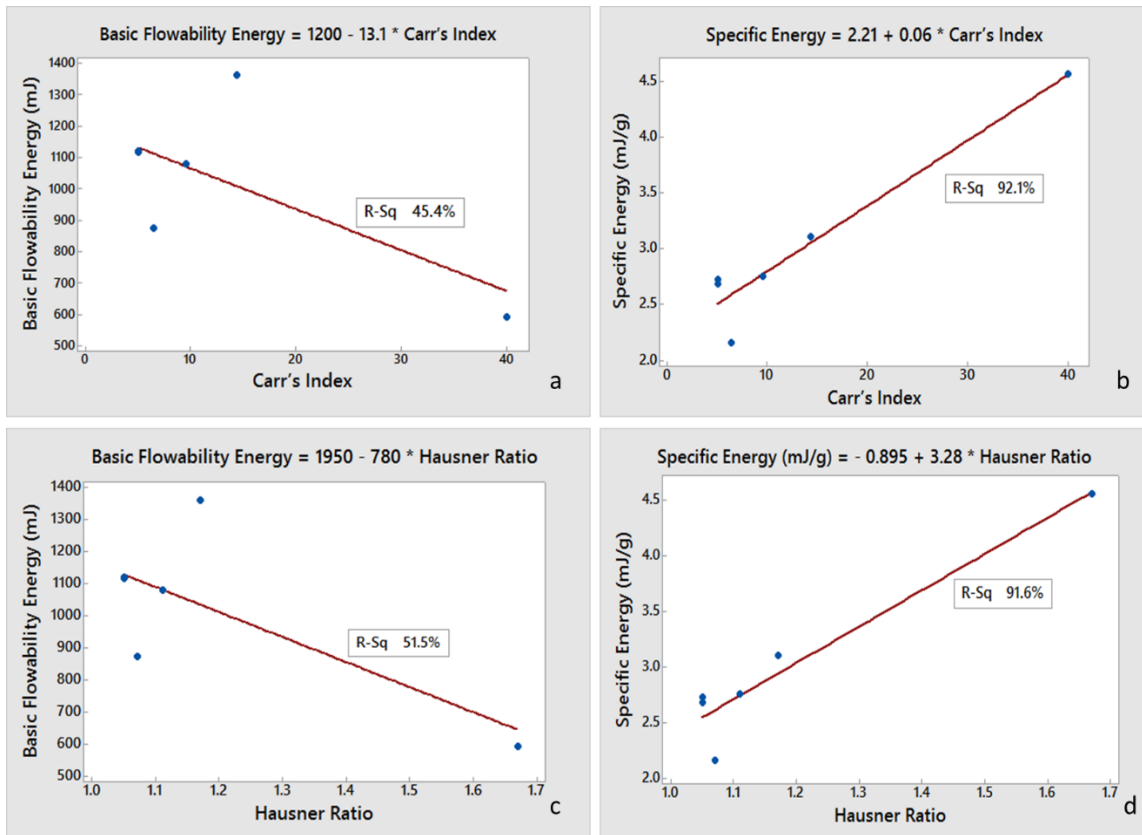


**Figure 17.** a) Linear fit plot for CI vs BFE b) Linear fit plot for CI vs SE c) Linear fit plot for HR vs BFE d) Linear fit plot for HR vs SE

#### 4.6. Shear cell measurements

The average of the FFC values for each combination of particle size and moisture content combinations from 3 runs were obtained. These FFC values were then plotted against the respective moisture percentages and the curve was fitted through these data points. The FFC values for each particle size range and the respective equation of the fitted curve are presented in Table 6 (a) & (b). Tables (a) and (b) represented the particle size ranges that were used in the study and the ones that were excluded, respectively.

The fitted curves thus obtained were of the following form:

$$\text{FFC} = (\text{Coefficient of Particle Size})(\text{Constant})^{\frac{1}{(\text{Moisture Percentage})}} \quad (10)$$

The ‘constant’ term in the set of equations in Table 6 was observed to lie between 0.96 and 1.25. Values between these two limits were iteratively examined for best fit, and it was found that a value of 1.15 gave the most accurate values of FFC for the different combinations of particle size and moisture percentages used in the study.

In Eq. 10, it was found that the first term varied significantly as the particle size was changed from test specimen to test specimen. This term was decided to be called the ‘coefficient of particle size’. To obtain its relationship with the particle size, this coefficient from each equation was plotted against the surface area mean diameters, respectively. A linear regression line was developed to fit the data, as shown in **Fig. 18**. The fit obtained displayed a correlation coefficient value of 0.94, showing very good agreement with the data. The equation of the linear regression obtained from the plot in **Fig. 18**. is given as:

$$\text{Coefficient of particle size} = 1.28 + 0.1 * D[3,2] \quad (11)$$

Here, D[3,2] is the surface area mean diameter of the particles. This equation was then used to incorporate the effect of varying surface area mean diameters of the particles into the equation being developed.

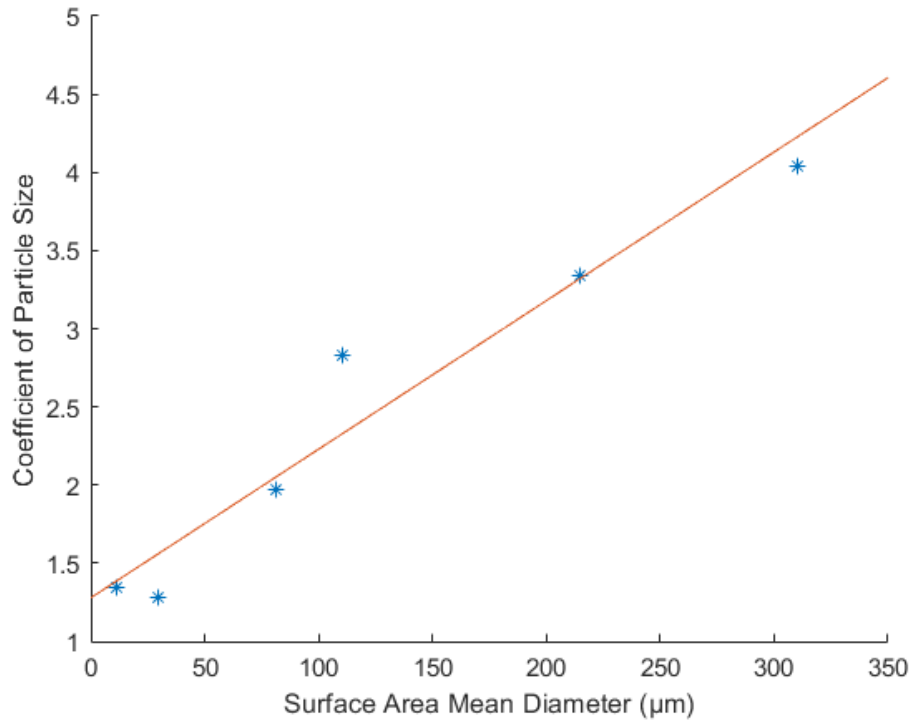


**Figure 18.** Coefficient of particle size plotted against the surface area mean diameters. A linear regression line is used to fit the data to develop a relationship between the two factors. The goodness of fit was evaluated by  $R^2$  value that was found to be 0.94.

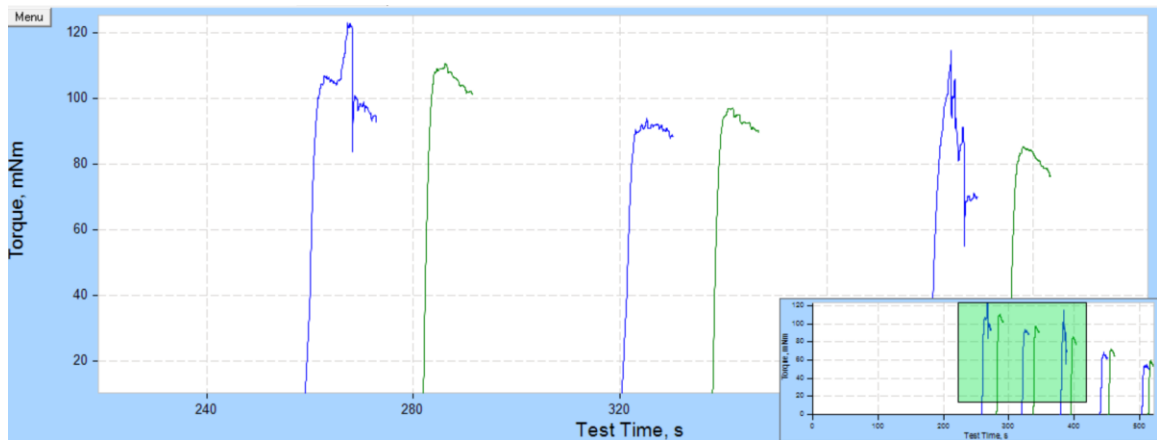
Table 6

- a) *Results from the shear cell tests of the bulk solids that were used in the study, averaged over 3 runs for each particle size range and moisture content combination. The standard deviation of the average values of FFC is also shown.*
- b) *Results from the shear cell test of bulk solids that were excluded from the study after initial testing, averaged over 3 runs for each particle size range and moisture content combination. The standard deviation of the average values of FFC is also shown.*

Particle Size	Moisture %	Avg. FFC value + Std. Dev	Equation of Fitted Curve	
5-11 µm D [3,2] = 11.4 µm	0.5 1 5 10 15	1.25 ± 0.01 1.30 ± 0.03 1.32 ± 0.05 1.33 ± 0.08 1.37 ± 0.10	FFC1= 1.35* (0.96 <sup>1/x</sup> )	
25-50 µm	0.5	1.48 ± 0.06		FFC2 = 1.28*(1.08 <sup>1/x</sup> )

D [3,2] = 29.7 μm	1 5 10 15	1.46 ± 0.01 1.33 ± 0.00 1.25 ± 0.00 1.27 ± 0.01	
70-100 μm D [3,2] = 81.5 μm	0.5 1 5 10 15	2.67 ± 0.03 2.49 ± 0.03 2.12 ± 0.08 1.97 ± 0.03 1.85 ± 0.02	FFC3 = 1.97*(1.18^(1/x))
120-180 μm D [3,2] = 110.0 μm	0.5 1 5 10 15	3.84 ± 0.18 3.43 ± 0.09 3.16 ± 0.03 2.80 ± 0.05 2.65 ± 0.08	FFC4 = 2.83*(1.17^(1/x))
180-250 μm D [3,2] = 215.0 μm	0.5 1 5 10 15	5.09 ± 0.42 4.36 ± 0.20 3.59 ± 0.04 3.31 ± 0.05 3.55 ± 0.14	FFC5 = 3.43*(1.23^(1/x))
250-355 μm D [3,2] = 310.0 μm	0.5 1 5 10 15	5.19 ± 0.28 5.02 ± 0.94 4.58 ± 0.19 3.71 ± 0.08 3.83 ± 0.52	FFC6 = 4.04*(1.25^(1/x))
<b>Particle Size</b>	<b>Moisture %</b>	<b>Avg. FFC value + Std. Dev</b>	<b>Equation of Fitted Curve</b>
430-600 μm	0.5 1 5 10 15	8.68 ± 2.06 8.74 ± 4.90 5.98 ± 1.78 4.12 ± 0.70 5.28 ± 3.89	FFC7 = (5.3)*(1.32)^(1/x)
600-850 μm	0.5 1 5 10 15	7.45 ± 2.26 9.67 ± 8.95 8.40 ± 8.09 1.00 ± 1.53 7.55 ± 7.59	FFC8 = (15.4)*(1.12)^(1/x)

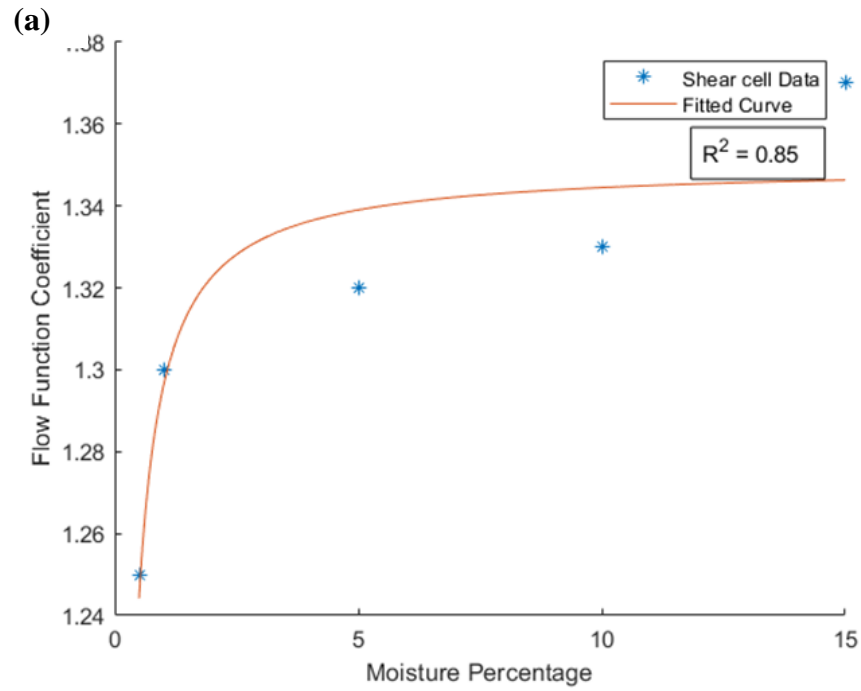
The particles in the size range of 430-600 microns and 600-850 microns were excluded from the study after initial testing, as the standard deviation of the average values of FFC obtained from these size ranges were too high across all moisture percentages (see Table 6b). Further proof for unreliability was decided by comparing the torque values for 250 – 355 micron and 430 – 600 microns at 0.5% moisture level. When the particles are too large or have agglomerates, there is a possibility of a sharp instantaneous drop in torque value, caused by slippage of the material. In this scenario, instead of creating a shear zone, the entire powder column rotates, producing unreliable data. This could be attributed to the physical constraints of the size of the shear cell, because of which the particle size of about 355 microns was decided to be the upper limit for the FT4 Powder Rheometer in this work. An instance where the torque values dropped for particles with 430-600 microns is shown in **Fig. 19**.

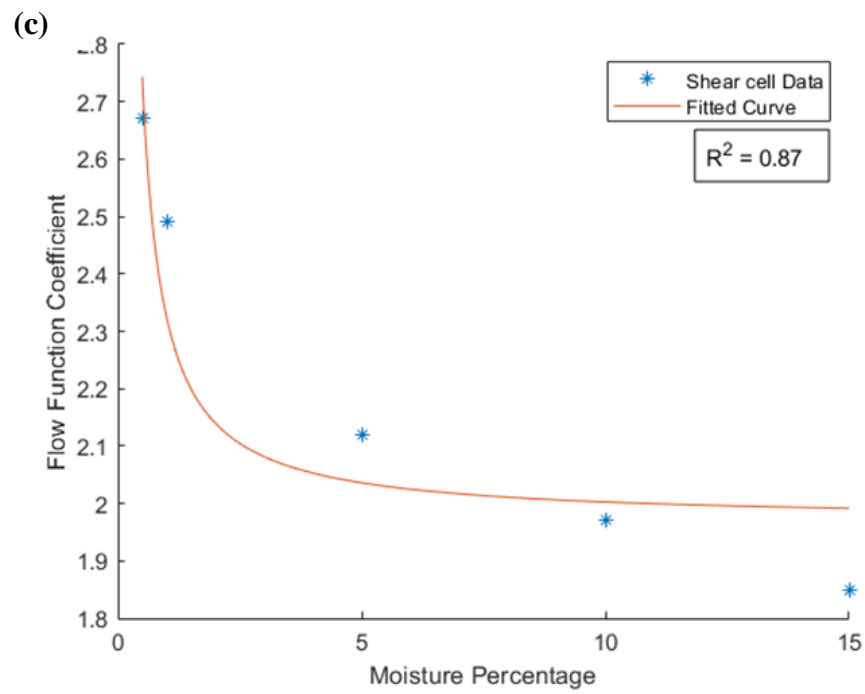
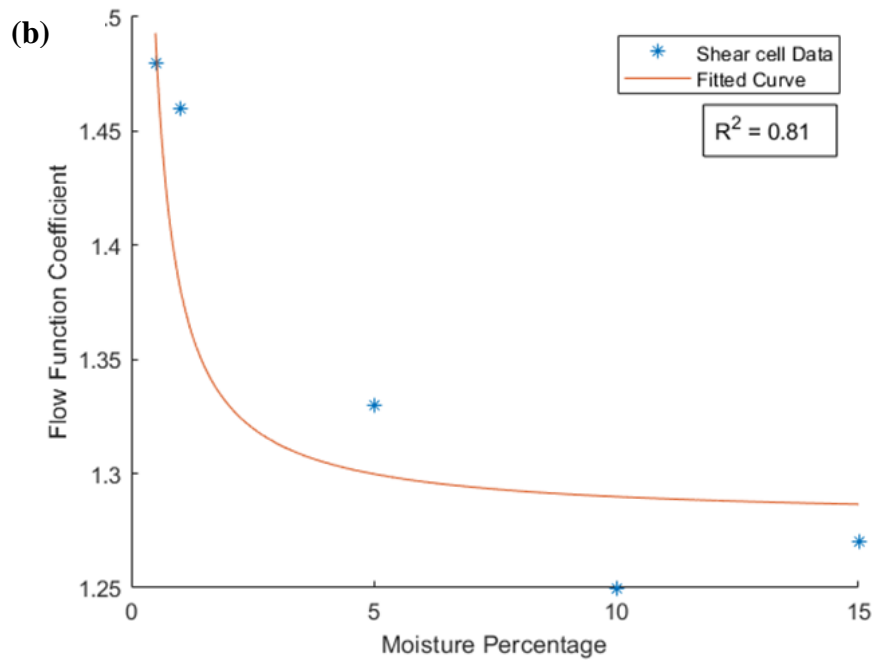


**Figure 19.** Torque values for 250-355 (green) and 430-600 (blue) micron glass beads with 0.5% moisture. The 430 – 600 micron particles with peaks demonstrate slippage in material.

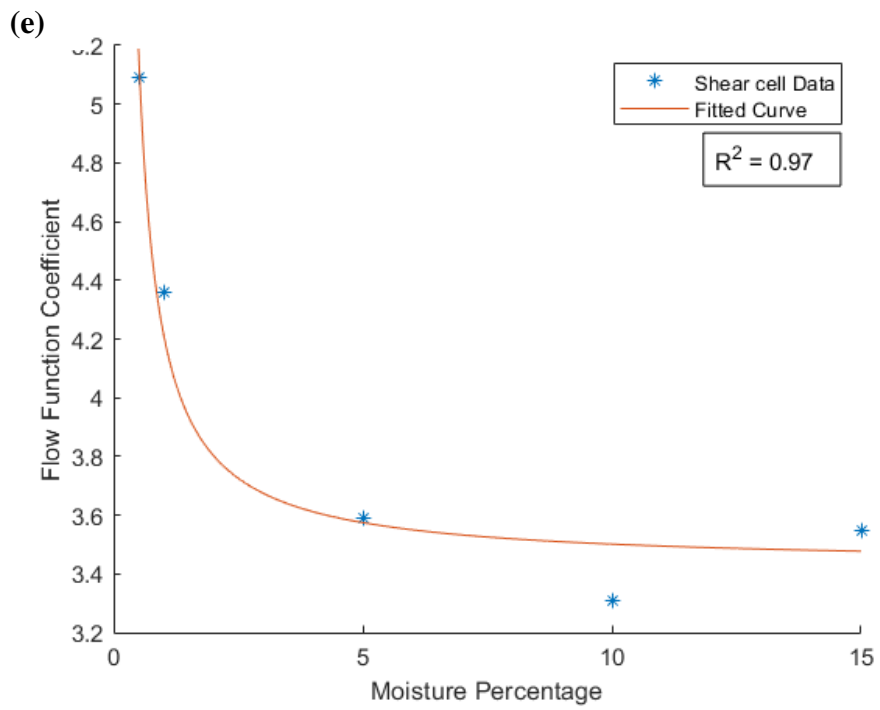
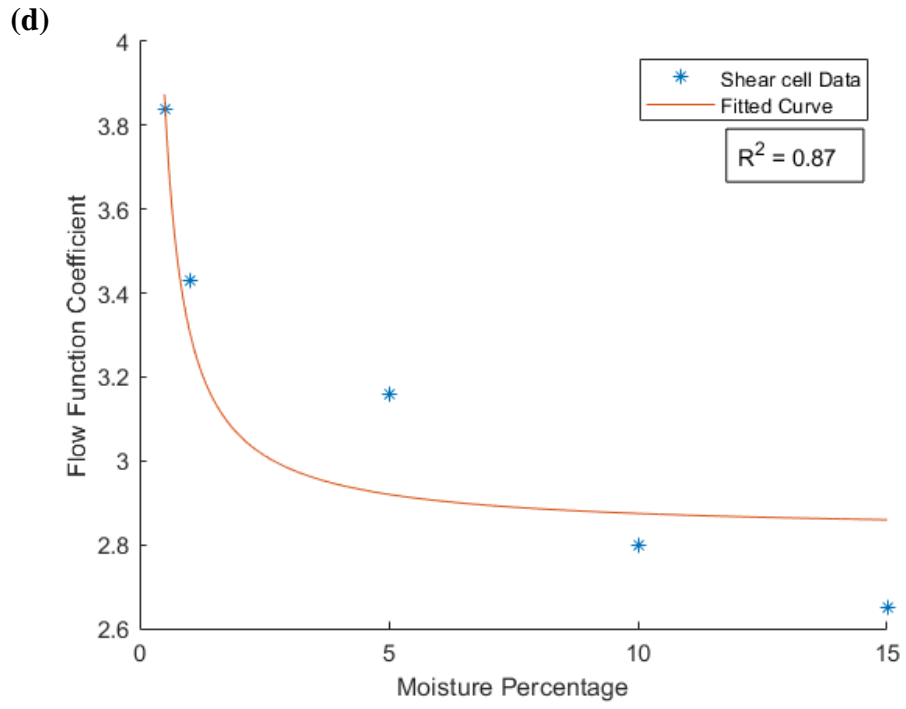
Considering the remaining particle size ranges, the average FFC values obtained were plotted against the moisture percentages for each size range. A data analysis and

visualization software, CurveExpert Pro, was then used to find a curve that best fit these. The goodness of fit was evaluated by taking the  $R^2$ -value as the metric (see **Figs. 20 (a) – (f)**). It was observed that the data points were most accurately represented by equations of the *power-root* type.









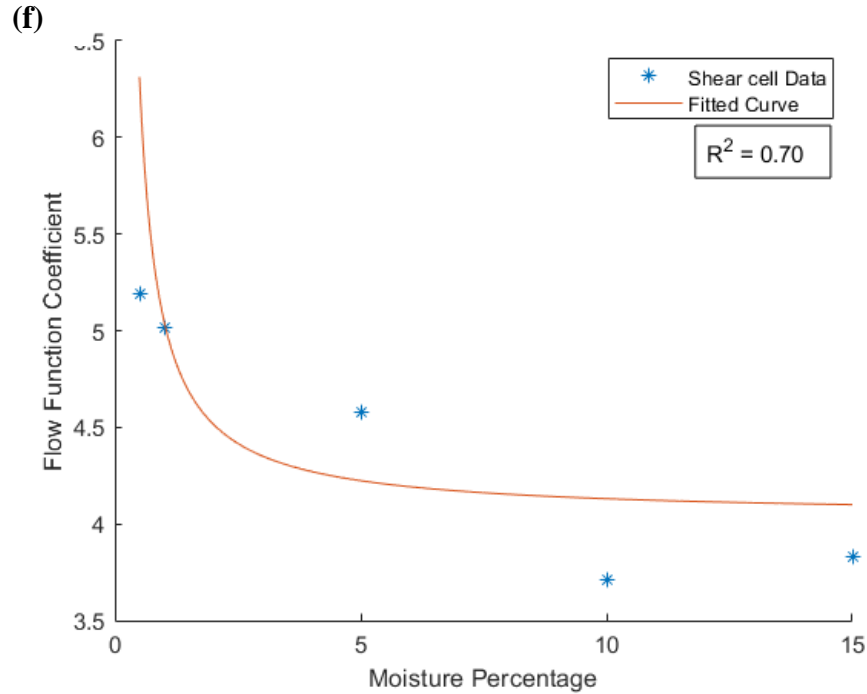


**Figure 20.** Fitted curves for shear cell data of glass beads for various moisture percentages. The corresponding PSDs are *a)* 5-11  $\mu\text{m}$  *b)* 25-50  $\mu\text{m}$  *c)* 70-100  $\mu\text{m}$  *d)* 120-180  $\mu\text{m}$  *e)* 180-250  $\mu\text{m}$  *f)* 250-355  $\mu\text{m}$

We can see that the FFC value consistently decreases in all cases as the moisture percentage increases, except in the case of the 5-11 microns size range. This can be explained by the fact that in the case of very fine particles, the interparticle interaction is dominated by Van der Waals forces, and thus the corresponding curve (**Fig. 20 (a)**) for the fine powder starts with very low values of FFC of 1.25 and 1.3, which indicate a very cohesive flow of the material. Gradually, as the moisture percentage increases, the formation of tiny liquid bridges dissipates this effect, and the moisture starts acting as a lubricant, thus improving the flowability relative to the initial conditions.

For the larger size ranges, the Van der Waals forces are not as strong, and the particles are relatively free-flowing. The addition of liquid to these particles led to the formation of

liquid bridges between the glass beads, and this introduced bonding forces between the particles. As the liquid percentage increased and the interparticle voids started being occupied by the liquid, surface tension forces and capillary pressure could have come into play and made the bulk solid much more cohesive, thus negatively impacting the flowability. This was indicated by FFC values dropping in Table 6a.

The main goal of this study was to develop a model that could take into account the varying particle sizes and the moisture percentage in a bulk solid and then predict the flow function coefficient for the same. The effect of the varying particle size was incorporated in the final model by substituting the function acquired in Eq. 10 into Eq. 11. The final equation obtained is as follows:

$$\text{FFC} = (1.28 + 0.1D_{3,2})(1.15^{\frac{1}{\text{moisture percentage}}}) \quad (12)$$

where FFC is the flow function coefficient and  $D_{3,2}$  is the surface area mean diameter in microns.

Eq. 12 was then used to make predictions for the FFC of different particle size-moisture content combinations. These predictions were then compared to experimentally obtained FFC values from shear cell tests performed on the FT4 Rheometer. The values predicted by the model were plotted against the values experimentally obtained from the shear cell tests, as shown in **Fig. 21**.

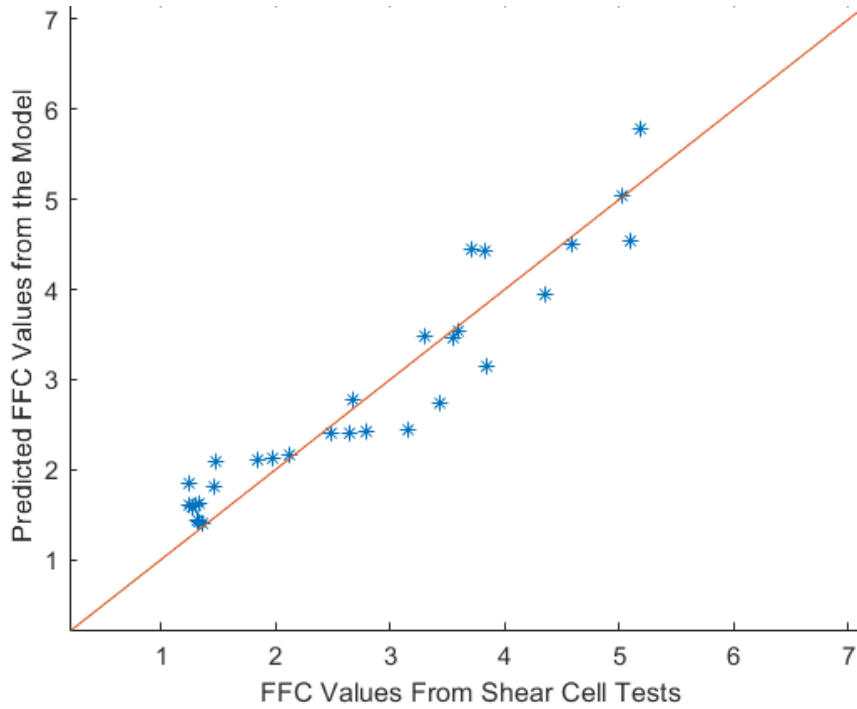


**Figure 21.** Correlation between the experimentally obtained values of the FFC and those predicted by the empirically developed model

As can be seen from **Fig. 21**, the predicted and the experimental values are very closely bunched together along the  $y=x$  line, showing very good agreement, with a correlation coefficient of 0.91.

## CHAPTER 5 IMPACT OF NON-SPHERICAL PROJECTILES ON DRY GRANULAR MEDIA

In this chapter, the findings for impact of non-spherical geometries on dry granular media are discussed. The effects of varying release heights, base surface area and the vertical length of projectiles are investigated using a power law approach. A comparative analysis for spherical projectiles and the non-spherical projectiles are discussed. The proposed equation is compared to the existing equations in the literature, and the improvements are showcased.

### ***5.1. Results and Discussion***

First, we conducted the impact experiments with the spherical projectile using the setup shown in **Fig. 11(b)** to validate the experimental procedure. **Fig. 22** shows the experimental penetration depth,  $d_{exp}$ , of a sphere compared with the theoretical penetration depth,  $d_{Eq.2}$ , obtained from Eq. (3). Both follow a similar trend, where the  $d$  value increases with an increase in release height. According to the results, there is only a 5.7% deviation, on average, between the theoretical and experimental penetration depths. Thus, the same methodology was applied for all experiments.

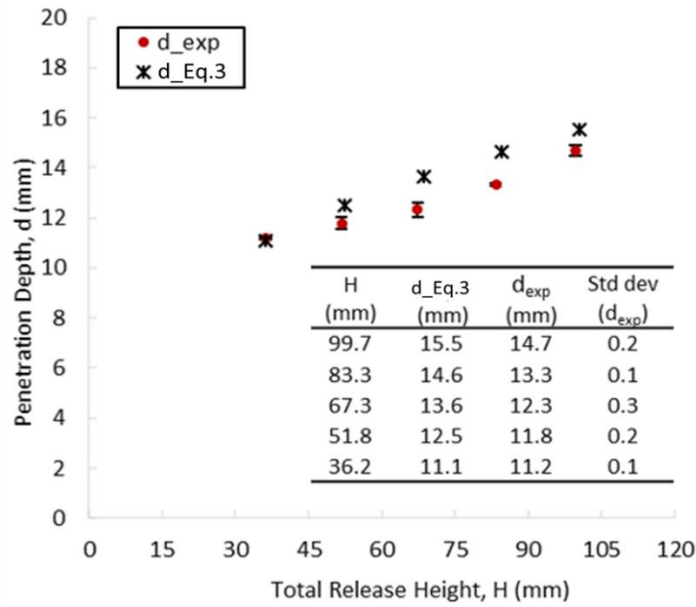


**Figure 22.** Experimental and theoretical penetration depths of spherical projectiles. (Inset) Tabulated values.  $H$  represents the total release height, which is the sum of the release height,  $h$ , and the experimental penetration depth,  $d_{exp}$ .

A power law relation between penetration depth,  $d$ , and each considered projectile parameter (e.g., vertical length,  $l$ , release height,  $h$ , and cross-sectional area of the base,  $A$ ) was investigated using the experimental findings of non-spherical impacts. In all of the experimental setups, including the previous works discussed with Eq. (3) - Eq. (5) and the current work, the granular target is non-cohesive and dry. Hence, similar to the formerly established models, it was assumed that the scaling between the density of the target bed and the penetration depth remains the same, irrespective of projectile shape. According to this assumption, it is the projectile properties that primarily affect the penetration depth, not the target material, as long as the particles are homogenous, spherical, and non-cohesive. Eq. (5) is the only relation among previous work that is applicable to complex shapes, which considers the surface area,  $A$ , in contact with the granular medium. However,

it does not consider the vertical length of the projectile,  $l$ . Eq. (5) is formulated assuming that the power law for spherical projectiles ( $d \sim H^{1/3}$ ) holds true for non-spherical geometries. However, for our experiments, there is a deviation in the analysis for both surface area and release height. Thus, we propose the following empirical relation:

$$d = \frac{0.14}{\mu} \left[ \rho_n \left( \frac{1}{2} \right) l^{\frac{3}{4}} h^{\frac{4}{5}} A^{\frac{-3}{4}} \right] \quad (13)$$

where  $\mu$  is the internal coefficient of friction of dry granular material,  $l$  is the vertical length of the projectile,  $h$  is the release height, and  $A$  is the surface area of the projectile base hitting the target. Eq. (13) considers the distance traveled by the projectile right before hitting the target, allowing the direct calculation of penetration depth. To derive Eq. (13), we used experimental data to calculate the power law between the penetration depth,  $d$ , and each variable considered ( $l$ ,  $h$ ,  $A$ ). We adjusted the powers to the closest fractional representation to obtain a dimensionally valid equation. For granular target properties,  $\mu$  and  $\rho_n$ , the scaling was assumed to be the same as for previous equations.

The penetration depths obtained for differently shaped geometries for sets A, B, C and D are shown in **Fig. 23**. The penetration depths ( $d$ ) of these geometrics were taken with respect to their release heights.

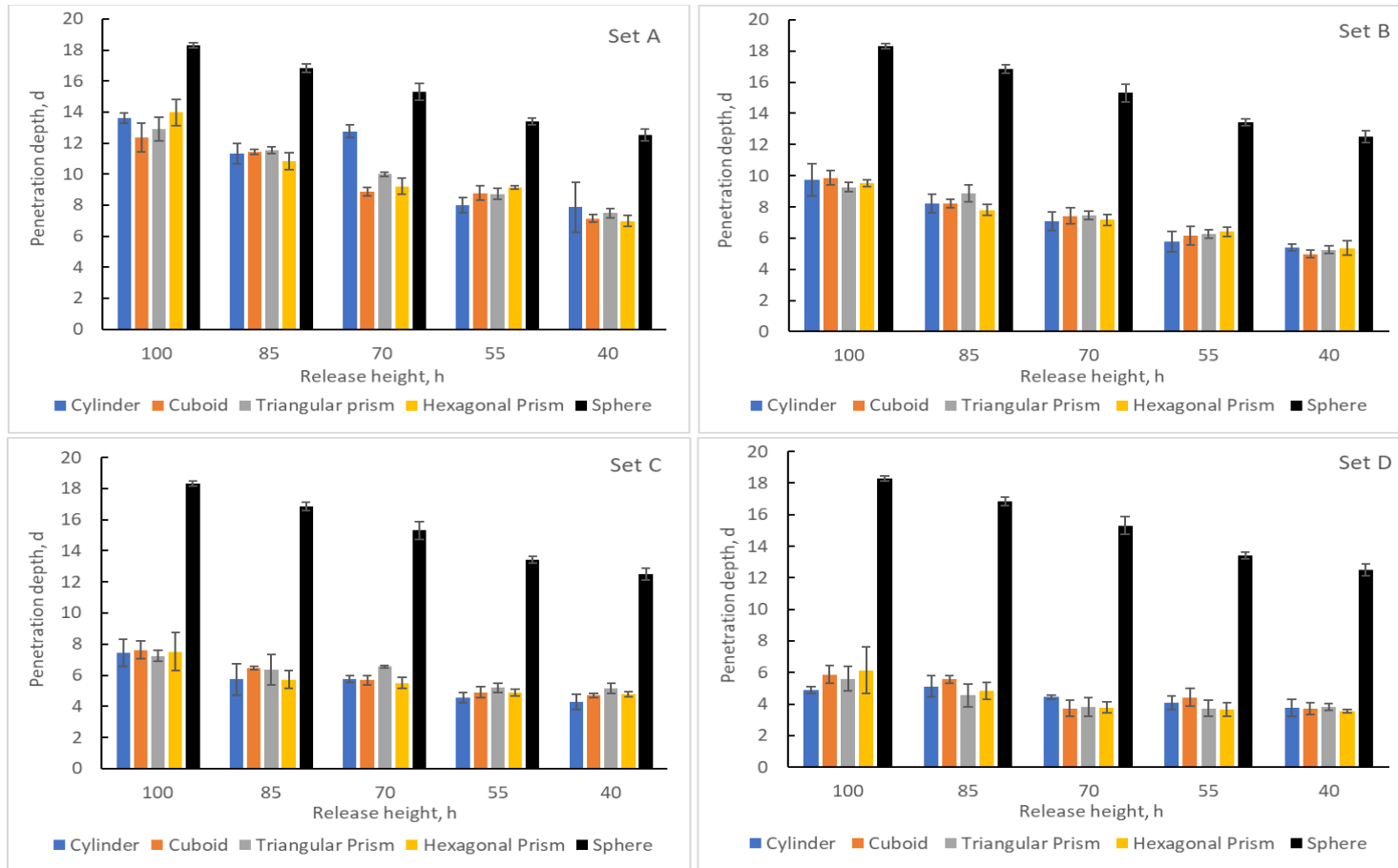


**Figure 23.** Penetration depths of various projectile geometries as a function of release height.



Analysis of Variance (ANOVA) is used here to study and compare the means of the population. In our study, four different shapes are used to study their effects with respect to  $d$ . Hence,  $d$  is the response variable, with four different factor levels. Since there is only one factor under study, one-way ANOVA was used in Minitab 18 to statistically analyze the data. The depth of each projectile shape (3 observations each) dropped from five different heights were considered as one set. Across each set, the surface area was the variable parameter. A significance level of 95% is used, which means that the corresponding inference about the data is true 95% of the time. The P-value in all of the cases is greater than the significance level (0.05). Hence, we conclude that the projectiles within the same set (with the same value of base surface area) penetrate equal distances when released from the same height, irrespective of shape. Raw data for the statistical analysis can be found in APPENDIX B.

As the release height of these projectiles is increased, the penetration depth also generally increases, due to the increased impact velocity. Thus, we conclude that the penetration depths of various geometries are independent of their shapes, as long as the base surface area, mass and density are held constant.

However, with a spherical projectile of equal mass and density, the base surface area encountering the granular target upon impact is not equal to that of relatively flat-surfaced geometries. For the same impact velocity, the spherical projectiles traveled deeper when compared to projectiles having a flat surface as an area of contact. With spherical projectiles, the contact surface upon initial impact is a single point, resulting in a higher impact force at a single spot on the target bed. However, for the other projectiles used in

this work, the base area that collides with the target is flat, and hence the force is distributed over an area rather than a single point. We expect these flat surfaces to result in a higher amount of drag force due to more material contact and consequently a shallower penetration.

**Fig. 24** shows a comparison between experimental penetration depth values of different projectiles used in this work for each release height and the penetration depth calculated using Eq. (4), Eq. (5) and Eq. (13). Like Eq. (3) and Eq. (4), Eq. (5) also considers the total release height,  $H$ , as one of the parameters, which requires prior knowledge of the penetration depth value in order to evaluate the equation. This prevents these equations from predicting the penetration depth. Eq. (13) predicted the  $d$  values close to the experimental data, while Eq. (4) and Eq. (5) slightly overestimated them. For Eq. (4), the range of penetration depths that agrees with the power law ( $d \sim H^{1/3}$ ) is greater than 0.5 inch, which is around 13 mm, while the highest tested  $d$  value is about 10 mm. Newhall & Durian (2003) proposed Eq. (5), which has limited experimental evidence with a predicted value of 67 mm for a deep footprint. Thus, Eq. (4) and Eq. (5) likely overestimate the data due to the relatively shallow penetration depths. However, irrespective of overestimation, all experimental and theoretical values follow a similar trend, where the depth of penetration increases with an increase in release height. Eq. (3), Eq. (4) and Eq. (5) concluded that the total release height,  $H$ , and penetration depth,  $d$ , follow a power law where  $d \sim H^{1/3}$ . In terms of total release height,  $H$ , which has been the traditional way of quantifying penetration depth, we observed the power law for non-spherical shallow impacts to be  $d \sim H^{3/4}$ . However, using  $H$  rather than  $h$  does not provide a dimensionally

valid relation for Eq. (13). Therefore, we derived the power law relation for release height,  $h$ , and penetration depth,  $d$ , as  $d \sim h^{4/5}$ . Additionally, the motivation behind Eq. (13) to predict penetration depth has been achieved by considering  $h$ .

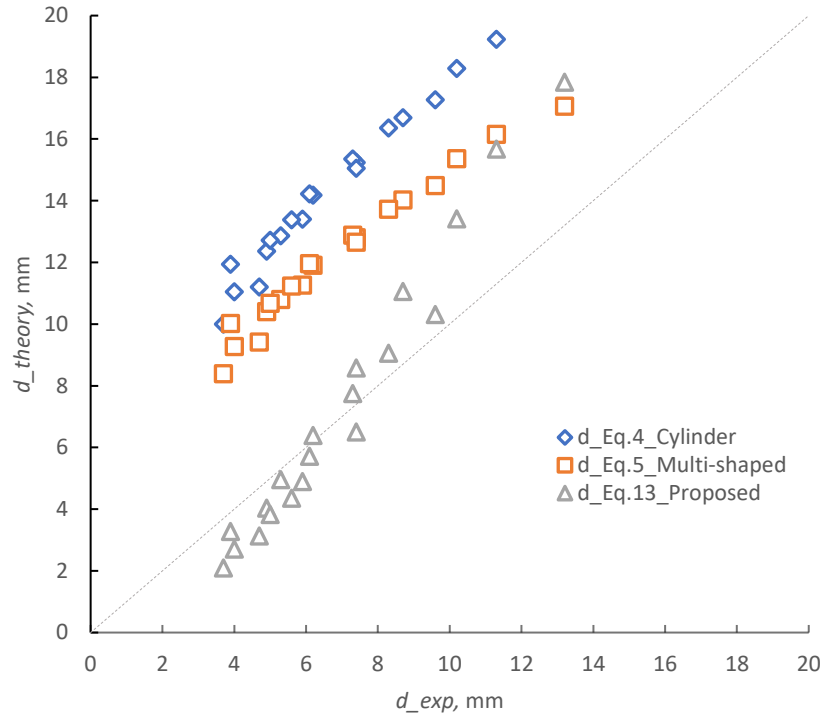


**Figure 24.** Comparison of theoretical penetration depth values calculated from Eq. (4) ( $d_{Eq.4\_cylinder}$ ), Eq. (5) ( $d_{Eq.5\_multi-shaped}$ ), and Eq. (13) ( $d_{Eq.13\_proposed}$ ) with the respective experimental values ( $d_{exp}$ ), and error bars indicating the standard deviation. In the data interpreted for  $d_{Eq.13\_proposed}$ , the average values of  $d$  for all three shapes (cylinder, cuboid and triangular prism) from each set was chosen for each release height.

Since the penetration depths for each set of projectiles with equal base surface areas were found to be equal in the experiments, the average penetration depth value of all shapes in each set for all release heights was plotted against theoretical values obtained from Eq. (13) (see **Fig 24**). The closeness of the data points to the equity line ( $y = x$ ) shows that the experimental values are very close to the theoretical ones.

The presented work eliminates the constraints of the existing literature equations (shape-specific dimensions like diameter, and using the total release height,  $H$ , which does not allow the prediction of penetration depth) by considering two important factors (see Eq. (13)), which include the surface area,  $A$ , encountering the target material upon impact and the vertical length of the projectile,  $l$ . Thus, the penetration depth for complex shapes can be evaluated when the contact area and vertical length are known. This equation can be applied to any type of geometry, irrespective of base shape and length, if the area of contact upon collision is not a single point. It was also assumed that the target material was dry and non-cohesive, and the penetration depths were shallow, where the  $d$  values were less than the radius of the projectiles. The established relation can serve as a preliminary tool to predict the penetration depths of projectiles with non-spherical geometries. Such data can be utilized to understand drag force experienced (Takita & Sumita, 2013) and depth of penetration traveled by objects interacting with granular media.

## CHAPTER 6 CONCLUSIONS AND FUTURE WORK

### ***6.1. Flowability Quantification of Glass Beads***

The particle and bulk properties of silica beads of various sizes were characterized. The following conclusions were drawn from the flowability experiments.

- Conventional flow descriptors of angle of repose, Carr's index and Hausner ratio were examined for glass beads of varying particle size. They could explain the flow regime of materials vaguely but could not differentiate the flow in confined and unconfined environments.
- Basic flowability energy and specific energy were studied, and the effect of varying particle size was investigated. There was an optimal size range of 125-180 microns that had a combination of desirable flow energy.
- Linear regression and statistical significance between conventional flow descriptors and basic flowability energy and specific energy indicated that confined flow was difficult to describe using angle of repose, Hausner ratio, and Carr's index.
- Effect of varying particle size (5 – 350 microns) and moisture percentages (0.5 – 15%) on the flow function coefficient (FFC) was studied, and an empirical relation was developed to predict FFC values in the pendular – capillary regime.

In the future, by including the following parameters, a stronger understanding on the flow regimes of various granular materials is possible.

- Study flow properties of non-ideal particles, such as biomass. Preliminary work on flowability experiments on two types of biomass samples can be found in APPENDIX A.
- More particle sizes and shapes should be investigated.
- Study the effects of aeration and consolidation on flow behavior of the materials.
- Improve the FFC model by studying more moisture levels.
- Incorporate a shape factor in FFC model.

### ***6.2. Projectile Impacts on Granular Media***

In the second part of this work, we tested the impact of non-spherical projectiles for various release heights and contact base areas and concluded the following.

- For the non-spherical impacts, there is a deviation from the power law established for spherical intruders.
- The penetration depth of projectiles having equal base surface areas is equal, irrespective of shape. This shows that the geometries of equal volume and density having an equal area of contact with the granular target experience a similar resistance and hence travel an equal depth, irrespective of shape.
- By investigating the power laws for factors such as base surface area, vertical length and release height, which affect the penetration depth of non-spherical projectiles, we proposed an empirical model that well represented experimental values, where the penetration depth scales with release height as  $d \sim h^{4/5}$ . This equation can be used to predict the penetration depth when the density, mass, and base surface area

of the projectile, and the density and volume fraction of the granular target are known.

For future work, it is important to validate the proposed model by testing out more complex geometries and incorporating different types of target materials.

## REFERENCES

- Abdullah, E. C., & Geldart, D. (1999). The use of bulk density measurements as flowability indicators. *Powder Technology*, 102(2). [https://doi.org/10.1016/S0032-5910\(98\)00208-3](https://doi.org/10.1016/S0032-5910(98)00208-3)
- Ambroso, M. A., Kamien, R. D., & Durian, D. J. (2005). Dynamics of shallow impact cratering. *Physical Review E - Statistical, Nonlinear, and Soft Matter Physics*, 72(4), 041305. <https://doi.org/10.1103/PhysRevE.72.041305>
- Amidon, G. E., Meyer, P. J., & Mudie, D. M. (2017). Particle, powder, and compact characterization. In *Developing Solid Oral Dosage Forms: Pharmaceutical Theory and Practice: Second Edition* (pp. 271–293). Elsevier Inc. <https://doi.org/10.1016/B978-0-12-802447-8.00010-8>
- Anderson, N., & Mitchell, D. (2016). Forest Operations and Woody Biomass Logistics to Improve Efficiency, Value, and Sustainability. *BioEnergy Research*, 9(2), 518–533. <https://doi.org/10.1007/s12155-016-9735-1>
- Baxter, T., & Prescott, J. (2017). Process development, optimization, and scale-up: Providing reliable powder flow and product uniformity. In *Developing Solid Oral Dosage Forms: Pharmaceutical Theory and Practice: Second Edition*. Elsevier Inc. <https://doi.org/10.1016/B978-0-12-802447-8.00026-1>
- Beakawi Al-Hashemi, H. M., & Baghabra Al-Amoudi, O. S. (2018). A review on the angle of repose of granular materials. *Powder Technology*, 330, 397–417. <https://doi.org/10.1016/J.POWTEC.2018.02.003>
- Bruni, G., Barletta, D., Poletto, M., & Lettieri, P. (2007). A rheological model for the flowability of aerated fine powders. *Chemical Engineering Science*, 62(1–2), 397–407. <https://doi.org/10.1016/j.ces.2006.08.060>
- Brzinski, T. A., Schug, J., Mao, K., & Durian, D. J. (2015). Penetration depth scaling for impact into wet granular packings. *Physical Review E - Statistical, Nonlinear, and Soft Matter Physics*, 91(2), 022202. <https://doi.org/10.1103/PhysRevE.91.022202>
- Chen, S., Adepu, M., Emady, H., Jiao, Y., & Gel, A. (2017). Enhancing the physical modeling capability of open-source MFIX-DEM software for handling particle size polydispersity: Implementation and validation. *Powder Technology*, 317, 117–125. <https://doi.org/10.1016/j.powtec.2017.04.055>
- Chum, H. L. (2015). *DOE Bioenergy Technologies Office (BETO) 2015 Project Peer Review*. 1–32.



- Clark, A. H., Petersen, A. J., Kondic, L., & Behringer, R. P. (2015). Nonlinear force propagation during granular impact. *Physical Review Letters*, *114*(14), 144502. <https://doi.org/10.1103/PhysRevLett.114.144502>
- Cleveland Vibrator Company. (2016). *Sizing Guide for Air and Electric Powered Vibrators for Hoppers, Bins and Chutes*.
- Coombes, J. R., & Yan, Y. (2015). Experimental investigations into the flow characteristics of pneumatically conveyed biomass particles using an electrostatic sensor array. *Fuel*. <https://doi.org/10.1016/j.fuel.2014.11.048>
- Crawford, N. C., Nagle, N., Sievers, D. A., & Stickel, J. J. (2016). The effects of physical and chemical preprocessing on the flowability of corn stover. *Biomass and Bioenergy*, *85*, 126–134. <https://doi.org/10.1016/j.biombioe.2015.12.015>
- Cui, H., & Grace, J. R. (2007). Pneumatic conveying of biomass particles: a review. *China Particuology*. [https://doi.org/10.1016/s1672-2515\(07\)60259-0](https://doi.org/10.1016/s1672-2515(07)60259-0)
- de Bruyn, J. R., & Walsh, A. M. (2004). Penetration of spheres into loose granular media. *Canadian Journal of Physics*, *82*(6), 439–446. <https://doi.org/10.1139/p04-025>
- Duran, J., & Behringer, R. P. (2001). Sands, Powders, and Grains: An Introduction to the Physics of Granular Materials. In *Physics Today* (Vol. 54). <https://doi.org/10.1063/1.1383168>
- Feng, Y., Blumenfeld, R., & Liu, C. (2019). Support of modified Archimedes' law theory in granular media. *Soft Matter*, *15*(14), 3008–3017. <https://doi.org/10.1039/c8sm02480d>
- Freeman, R. (2007). Measuring the flow properties of consolidated, conditioned and aerated powders - A comparative study using a powder rheometer and a rotational shear cell. *Powder Technology*, *174*(1–2), 25–33. <https://doi.org/10.1016/j.powtec.2006.10.016>
- Freeman, R. (2008). *Investigating the confined and unconfined flow behavior of powders*.
- Freeman, R. E., Cooke, J. R., & Schneider, L. C. R. (2009). Measuring shear properties and normal stresses generated within a rotational shear cell for consolidated and non-consolidated powders. *Powder Technology*, *190*(1–2), 65–69. <https://doi.org/10.1016/j.powtec.2008.04.084>
- FT4 Powder Rheometer - Dynamic Methodology*. (n.d.). Retrieved April 12, 2021, from <https://www.freemantech.co.uk/powder-testing/ft4-powder-rheometer-powder-flow-tester/dynamic-methodology>

- Fu, X., Huck, D., Makein, L., Armstrong, B., Willen, U., & Freeman, T. (2012). Effect of particle shape and size on flow properties of lactose powders. *Particuology*, *10*(2), 203–208. <https://doi.org/10.1016/j.partic.2011.11.003>
- Gnagne, E. H., Petit, J., Gaiani, C., Scher, J., & Amani, G. N. (2017). Characterisation of flow properties of foutou and fofou flours, staple foods in West Africa, using the FT4 powder rheometer. *Journal of Food Measurement and Characterization*, *11*(3), 1128–1136. <https://doi.org/10.1007/s11694-017-9489-2>
- Goldman, D. I., & Umbanhowar, P. (2008). Scaling and dynamics of sphere and disk impact into granular media. *Physical Review E - Statistical, Nonlinear, and Soft Matter Physics*, *77*(2), 1–14. <https://doi.org/10.1103/PhysRevE.77.021308>
- Grima, A., Hastie, D., Curry, D., Wypych, P., & Roche, R. La. (2011). The beginning of a new era in design: Calibrated discrete element modelling. *Faculty of Engineering and Information Sciences - Papers: Part A*, *16*(October), 14–21. <https://doi.org/10.3390/ijgi5030023>
- Grima, A. P., Fraser, T., & Hastie, D. B. (2011). Discrete element modelling : trouble-shooting and optimisation tool for chute design. *Beltcon 16, May 2018*, 1–26.
- Hare, C., Zafar, U., Ghadiri, M., Freeman, T., Clayton, J., & Murtagh, M. J. (2015). Analysis of the dynamics of the FT4 powder rheometer. *Powder Technology*, *285*, 123–127. <https://doi.org/10.1016/j.powtec.2015.04.039>
- Hilbert, J. D., & Solt, P. E. (2008). *Pneumatic points to ponder* (Vol. 22, Issue March, pp. 21–27).
- Jan, S., Karde, V., Ghoroi, C., & Saxena, D. C. (2018). Effect of particle and surface properties on flowability of rice flours. *Food Bioscience*, *23*(March), 38–44. <https://doi.org/10.1016/j.fbio.2018.03.001>
- Jin, Y., Lu, H., Guo, X., & Gong, X. (2018). Effect of water addition on flow properties of lignite particles. *Chemical Engineering Research and Design*, *132*, 1020–1029. <https://doi.org/10.1016/j.cherd.2017.11.012>
- Katsuragi, H., & Durian, D. J. (2007). Unified force law for granular impact cratering. *Nature Physics*, *3*(6), 420–423. <https://doi.org/10.1038/nphys583>
- Khan, M. A. (2015). Mechanics of projectile penetration into non-cohesive soil targets. *International Journal of Civil Engineering*, *13*(1). <https://doi.org/10.22068/IJCE.13.1.28>

- Koynov, S., Muzzio, F. J., & Glasser, B. J. (2016). A novel consolidation method to measure powder flow properties using a small amount of material. *AIChE Journal*, 62(12), 4193–4200. <https://doi.org/10.1002/aic.15321>
- Leturia, M., Benali, M., Lagarde, S., Ronga, I., & Saleh, K. (2014). Characterization of flow properties of cohesive powders: A comparative study of traditional and new testing methods. *Powder Technology*, 253, 406–423. <https://doi.org/10.1016/j.powtec.2013.11.045>
- Li, C., Zhang, T., & Goldman, D. I. (2013). A terradynamics of legged locomotion on granular media. *Science*, 339(6126), 1408–1412. <https://doi.org/10.1126/science.1229163>
- Lobo-Guerrero, S., & Vallejo, L. E. (2007). Influence of pile shape and pile interaction on the crushable behavior of granular materials around driven piles: DEM analyses. *Granular Matter*, 9(3–4), 241–250. <https://doi.org/10.1007/s10035-007-0037-3>
- Lu, H., Guo, X., Gong, X., Cong, X., Liu, K., & Qi, H. (2012). Experimental study on aerated discharge of pulverized coal. *Chemical Engineering Science*, 71, 438–448. <https://doi.org/10.1016/j.ces.2011.11.006>
- Lu, H., Guo, X., Jin, Y., & Gong, X. (2018). Effect of moisture on flowability of pulverized coal. *Chemical Engineering Research and Design*, 133, 326–334. <https://doi.org/10.1016/j.cherd.2018.03.023>
- Majid, I., & Nanda, V. (2017). Effect of sprouting on the physical properties, morphology and flowability of onion powder. *Journal of Food Measurement and Characterization*, 11(4), 2033–2042. <https://doi.org/10.1007/s11694-017-9586-2>
- Marston, J. O., Vakarelski, I. U., & Thoroddsen, S. T. (2012). Sphere impact and penetration into wet sand. *Physical Review E*, 86(2), 020301(R). <https://doi.org/10.1103/PhysRevE.86.020301>
- Martin Engineering. (n.d.). *Keep material flowing efficiently from start to finish*.
- Marvi, H., Gong, C., Gravish, N., Astley, H., Travers, M., Hatton, R. L., Mendelson, J. R., Choset, H., Hu, D. L., & Goldman, D. I. (2014). Sidewinding with minimal slip: Snake and robot ascent of sandy slopes. *Science*, 346(6206), 224–229. <https://doi.org/10.1126/science.1255718>
- Mass flow and funnel flow hoppers*. (n.d.). Retrieved April 9, 2021, from [https://www.powderprocess.net/mass\\_flow\\_silo.html](https://www.powderprocess.net/mass_flow_silo.html)
- Mehos, G., Eggleston, M., Grenier, S., Malanga, C., Shrestha, G., & Trautman, T. (2018).

Designing hoppers, bins, and silos for reliable flow. *Chemical Engineering Progress*, 114(4).

- Mitra, H., Pushpadass, H. A., Franklin, M. E. E., Ambrose, R. P. K., Ghoroi, C., & Battula, S. N. (2017). Influence of moisture content on the flow properties of basundi mix. *Powder Technology*, 312, 133–143.  
<https://doi.org/10.1016/j.powtec.2017.02.039>
- Mitsubishi Chemical Advanced Materials. (n.d.). *System TIVAR® Engineering Solutions for Bulk Material Flow Problems*.
- Nan, W., Ghadiri, M., & Wang, Y. (2017a). Analysis of powder rheometry of FT4: Effect of air flow. *Chemical Engineering Science*, 162, 141–151.  
<https://doi.org/10.1016/j.ces.2017.01.002>
- Nan, W., Ghadiri, M., & Wang, Y. (2017b). Analysis of powder rheometry of FT4: Effect of particle shape. *Chemical Engineering Science*, 173, 374–383.  
<https://doi.org/10.1016/j.ces.2017.08.004>
- Nazhat, Y., & Airey, D. (2015). The kinematics of granular soils subjected to rapid impact loading. *Granular Matter*, 17(1), 1–20. <https://doi.org/10.1007/s10035-014-0544-y>
- Newhall, K. A., & Durian, D. J. (2003). Projectile-shape dependence of impact craters in loose granular media. *Physical Review E - Statistical, Nonlinear, and Soft Matter Physics*, 68(6), 603011–603013. <https://doi.org/10.1103/PhysRevE.68.060301>
- Nordstrom, K. N., Lim, E., Harrington, M., & Losert, W. (2014). Granular dynamics during impact. *Physical Review Letters*, 112(22), 228002.  
<https://doi.org/10.1103/PhysRevLett.112.228002>
- Opaliński, I., Chutkowski, M., & Stasiak, M. (2012). Characterizing moist food-powder flowability using a Jenike shear-tester. *Journal of Food Engineering*, 108(1), 51–58.  
<https://doi.org/10.1016/j.jfoodeng.2011.07.031>
- Peng, Y., Wu, H., Fang, Q., & Kong, X. Z. (2019). Modified spherical cavity-expansion model for projectile penetration into concrete targets. *Acta Mechanica Sinica/Lixue Xuebao*, 35(3), 518–534. <https://doi.org/10.1007/s10409-018-0815-7>
- Prescott, J. K., & Barnum, R. A. (2001). On powder flowability: Part I. In *Pharmaceutical Technology Europe* (Vol. 13, Issue 1, p. 236 [14 p.]).
- Reimold, W. U. (1996). Impact cratering: A geologic process. In *Earth-Science Reviews* (Vol. 41, Issues 3–4). [https://doi.org/10.1016/S0012-8252\(96\)00035-9](https://doi.org/10.1016/S0012-8252(96)00035-9)

- Roberts, a. W., & Scott, O. J. (1992). Chute Design Considerations for Feeding and Transfer. *Conveyor Transfer Chute Design in Modern Concepts in Belt Conveying and Handling Bulk Solids*, 1–22.
- Rohilla, L., Garg, V., Mallick, S. S., & Setia, G. (2018). An experimental investigation on the effect of particle size into the flowability of fly ash. *Powder Technology*, 330, 164–173. <https://doi.org/10.1016/j.powtec.2018.02.013>
- Saw, H. Y., Davies, C. E., Paterson, A. H. J., & Jones, J. R. (2015). Correlation between powder flow properties measured by shear testing and Hausner ratio. *Procedia Engineering*, 102, 218–225. <https://doi.org/10.1016/j.proeng.2015.01.132>
- Seguin, A., Bertho, Y., & Gondret, P. (2008). Influence of confinement on granular penetration by impact. *Physical Review E - Statistical, Nonlinear, and Soft Matter Physics*, 78(1), 1–4. <https://doi.org/10.1103/PhysRevE.78.010301>
- Sharpe, S. S., Kuckuk, R., & Goldman, D. I. (2015). Controlled preparation of wet granular media reveals limits to lizard burial ability. *Physical Biology*, 12(4), 46009. <https://doi.org/10.1088/1478-3975/12/4/046009>
- Shi, H., Mohanty, R., Chakravarty, S., Cabisco, R., Morgeneyer, M., Zetzener, H., Ooi, J. Y., Kwade, A., Luding, S., & Magnanimo, V. (2018). Effect of particle size and cohesion on powder yielding and flow. *KONA Powder and Particle Journal*, 2018(35), 226–250. <https://doi.org/10.14356/kona.2018014>
- Søgaard, S., Bryder, M., Allesø, M., & Rantanen, J. (2019). *Characterization of powder properties using a powder rheometer*. 11(1), 825. <https://doi.org/10.3390/ecps2012-00825>
- Takita, H., & Sumita, I. (2013). Low-velocity impact cratering experiments in a wet sand target. *Physical Review E - Statistical, Nonlinear, and Soft Matter Physics*, 88(2), 1–10. <https://doi.org/10.1103/PhysRevE.88.022203>
- Tannous, K., Lam, P. S., Sokhansanj, S., & Grace, J. R. (2013). Physical properties for flow characterization of ground biomass from douglas fir wood. *Particulate Science and Technology*, 31(3), 291–300. <https://doi.org/10.1080/02726351.2012.732676>
- Tapia, F., Espíndola, D., Hamm, E., & Melo, F. (2013). Effect of packing fraction on shear band formation in a granular material forced by a penetrometer. *Physical Review E - Statistical, Nonlinear, and Soft Matter Physics*, 87(1), 014201. <https://doi.org/10.1103/PhysRevE.87.014201>
- Thalberg, K., Lindholm, D., & Axelsson, A. (2004). *Comparison of different flowability*

tests for powders for inhalation. *146*, 206–213.  
<https://doi.org/10.1016/j.powtec.2004.08.003>

- Trubetskaya, A., Poyraz, Y., Weber, R., & Wadenbäck, J. (2017). Secondary comminution of wood pellets in power plant and laboratory-scale mills. *Fuel Processing Technology*, *160*, 216–227. <https://doi.org/10.1016/j.fuproc.2017.02.023>
- Uehara, J. S., Ambroso, M. A., Ojha, R. P., & Durian, D. J. (2003). Low-speed impact craters in loose granular media. *Physical Review Letters*, *90*(19), 194301.

*Uniaxial Powder Tester – Micromeritics*. (n.d.). Retrieved March 2, 2021, from <https://www.micromeritics.com/uniaxial-powder-tester/>

USPC, U. S. P. C. (2014). Method II-Measurement in a Volumeter. *The United States Pharmacopeial Convention*, *06*(2012), 2014–2016.

Viana, H. F. dos S., Rodrigues, A. M., Godina, R., Matias, J. C. de O., & Nunes, L. J. R. (2018). Evaluation of the physical, chemical and thermal properties of Portuguese maritime pine biomass. *Sustainability (Switzerland)*, *10*(8), 1–15.  
<https://doi.org/10.3390/su10082877>

Wada, K., Senshu, H., & Matsui, T. (2006). Numerical simulation of impact cratering on granular material. *Icarus*, *180*(2), 528–545.  
<https://doi.org/10.1016/j.icarus.2005.10.002>

Wang, W., Zhang, J., Yang, S., Zhang, H., Yang, H., & Yue, G. (2010). Experimental study on the angle of repose of pulverized coal. *Particuology*, *8*(5), 482–486.  
<https://doi.org/10.1016/j.partic.2010.07.008>

Wilkinson, S. K., Turnbull, S. A., Yan, Z., Stitt, E. H., & Marigo, M. (2017). A parametric evaluation of powder flowability using a Freeman rheometer through statistical and sensitivity analysis: A discrete element method (DEM) study. *Computers and Chemical Engineering*, *97*, 161–174.  
<https://doi.org/10.1016/j.compchemeng.2016.11.034>

Wouters, I. M. F., & Geldart, D. (1996). Characterising semi-cohesive powders using angle of repose. *Particle and Particle Systems Characterization*, *13*(4), 254–259.  
<https://doi.org/10.1002/ppsc.19960130408>

Xu, G., Li, M., & Lu, P. (2019). Experimental investigation on flow properties of different biomass and torrefied biomass powders. *Biomass and Bioenergy*, *122*(January), 63–75. <https://doi.org/10.1016/j.biombioe.2019.01.016>

Yan, Y., Li, P., & Ji, S. (2013). Buffer capacity of granular matter to impact of spherical projectile based on discrete element method. *Frontiers of Architecture and Civil*

*Engineering in China*, 7(1), 50–54. <https://doi.org/10.1007/s11709-013-0186-x>

Zegzulka, J., Gelnar, D., Jezerska, L., Prokes, R., & Rozbroj, J. (2020). Characterization and flowability methods for metal powders. *Scientific Reports*, 10(1), 1–19. <https://doi.org/10.1038/s41598-020-77974-3>

Zhang, T., & Goldman, D. I. (2014). The effectiveness of resistive force theory in granular locomotion. *Physics of Fluids*, 26(10), 101308. <https://doi.org/10.1063/1.4898629>

APPENDIX A

FLOWABILITY DATA COLLECTED FOR BIOMASS SAMPLES



**Biomass samples used:**



**Figure A. 1.** Corn stover and pine forest residue fines produced from hammer milling

**Flow energy calculations for biomass:**

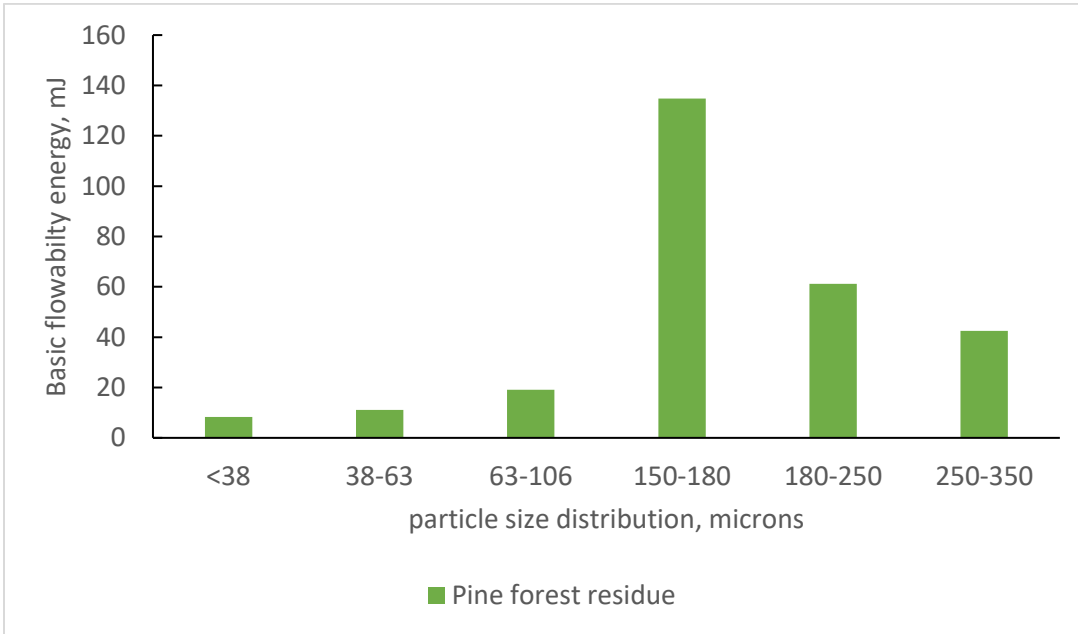


**Figure A. 2.** Effect of varying particle size distribution on Basic Flowability Energy (BFE) of pine forest residue

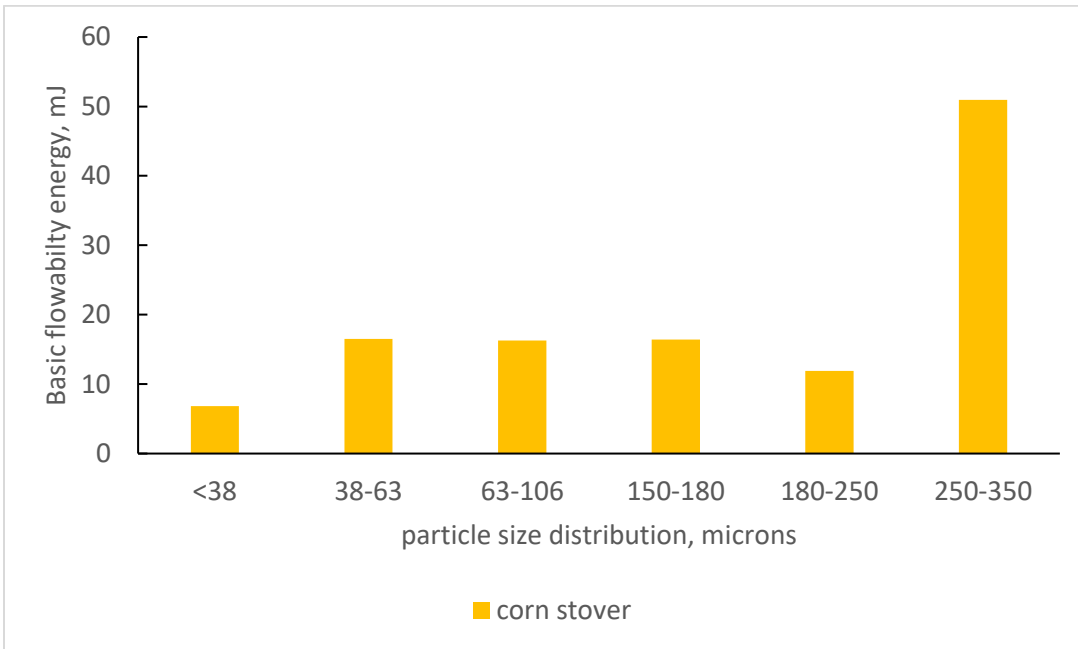


**Figure A. 3.** Effect of varying particle size distribution on Basic Flowability Energy (BFE) of pine forest residue

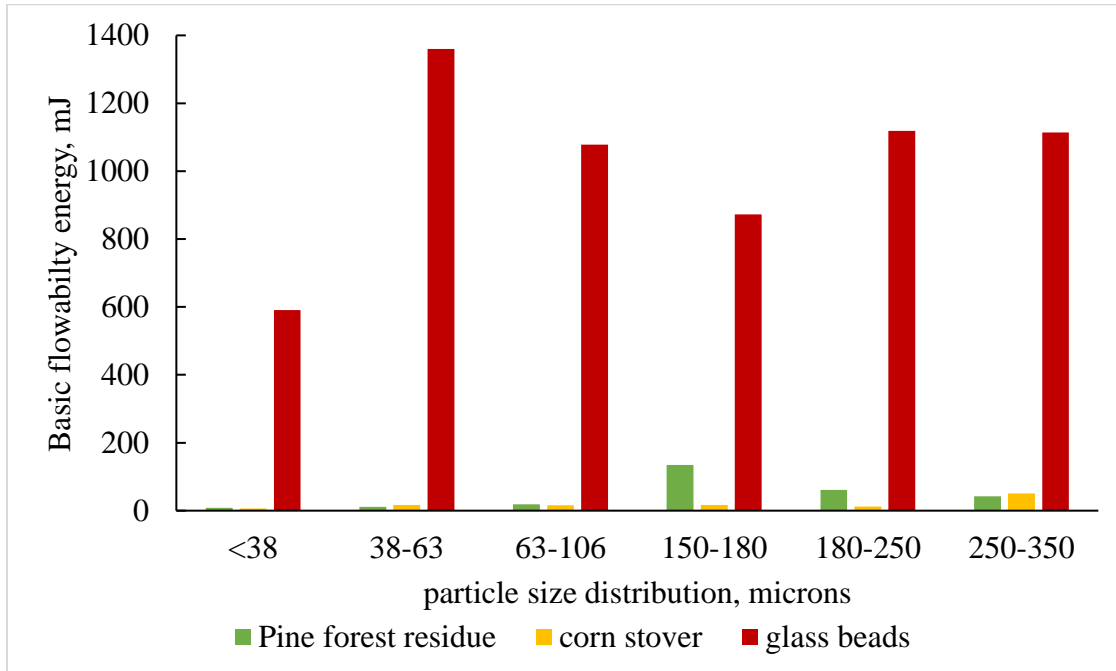


**Figure A. 4.** Comparison among BFE values of biomass samples and glass beads

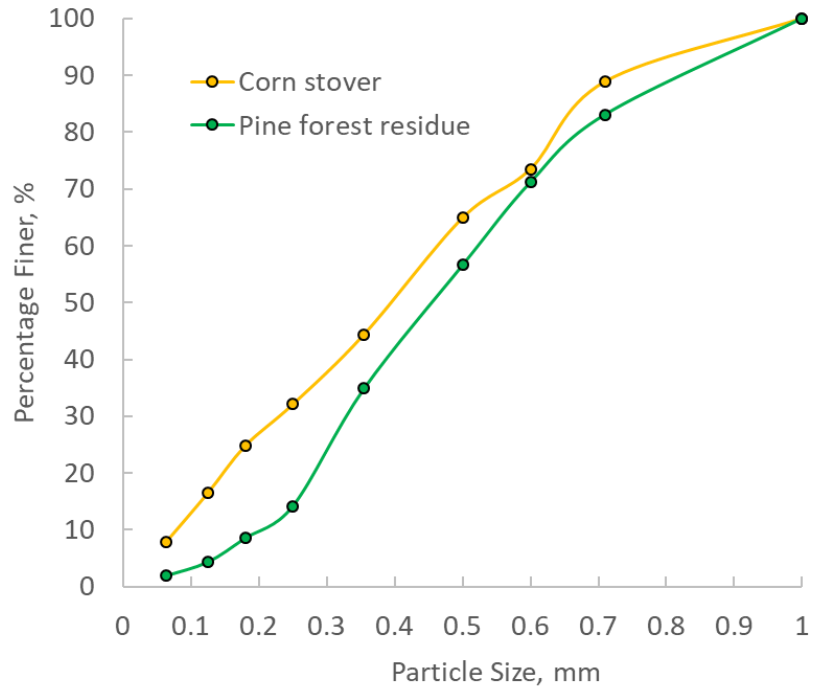


**Figure A. 5.** Particle size distribution analysis of corn stover and pine forest residue fines acquired from hammer milling (as-is)

Total Flow Energy tested for the following samples:

- i) sieved as-is samples of 250-355  $\mu\text{m}$  size range
- ii) as-is samples of unsorted size
- iii) oven-dried samples of unsorted dry corn stover and pine forest residue

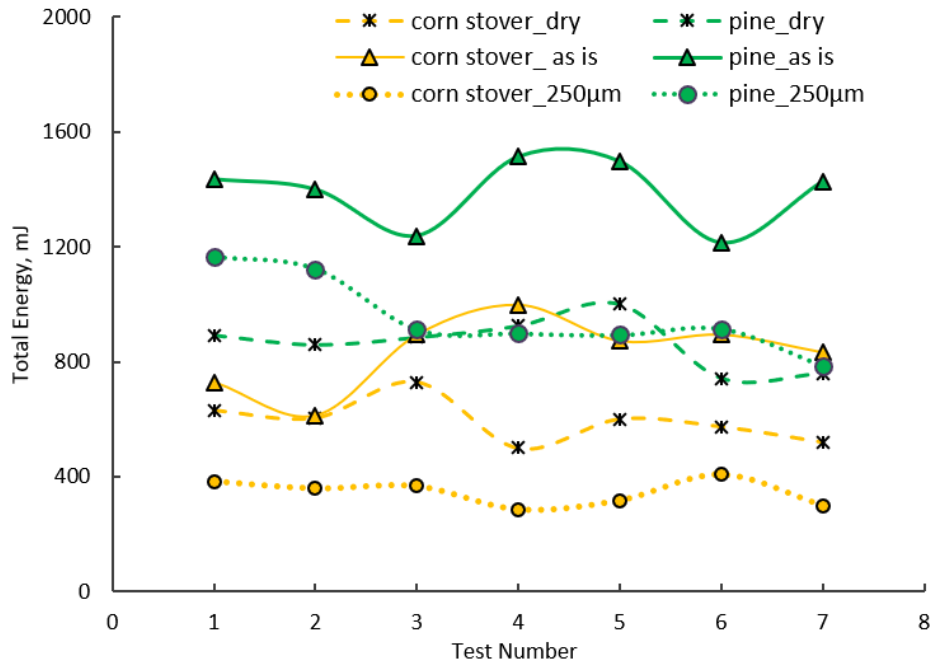


**Figure A. 6.** Total Energy (TE) of unsorted as-is, oven-dry, and sieved biomass samples. The test number on the x-axis indicates the number of times TE is measured per experiment. Before each test, the sample is conditioned to maintain a homogenous distribution of the material.

Pine forest residue as-is demonstrated the highest total energy, indicating that the material is the most poorly flowing compared to the others. However, after oven-drying, the flow energy of the pine forest residue drastically reduced. This trend is also observed in the corn stover samples, though the difference is not as dramatic. The sieved samples have also exhibited a considerable drop in total energy values, indicating that the particle size distribution (PSD) plays a significant role in flow behavior. More ranges of PSDs must be tested for different milling operations to determine a trend.

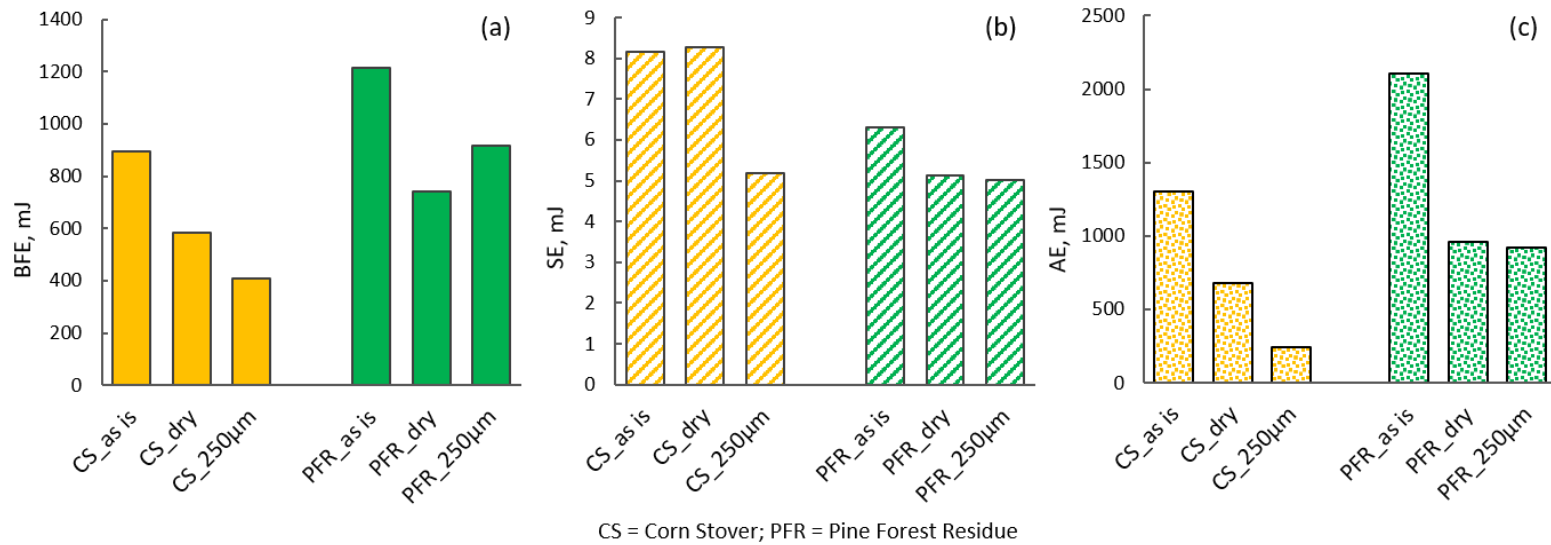


**Figure A. 7.** (a) Basic Flowability Energy (BFE), (b) Specific Energy (SE), and (c) Aerated Energy (AE), for as-is, oven-dried, and sieved biomass samples

### Method

Null hypothesis All means are equal  
Alternative hypothesis Not all means are equal  
Significance level  $\alpha = 0.05$

### Analysis of Variance

Source	DF	Adj SS	Adj MS	F-Value	P-Value
Factor	2	6.058	3.029	1.65	0.219
Error	18	32.994	1.833		
Total	20	39.052			

**Figure A. 8.** Analysis of Variance for angle of repose values obtained from the base method and the arc tangent method.

## APPENDIX B

### RAW DATA AND STATISTICAL ANALYSIS FOR IMPACT EXPERIMENTS

**Raw data on the penetration depths of various projectile geometries:**

Table B.4. Raw data for penetration depth of non-spherical geometries used in the study

<b>Set (A)</b>								
h (mm)	<b>Cylinder</b>		<b>Cuboid</b>		<b>Triangular Prism</b>		<b>Hexagonal Prism</b>	
	d (mm)	Std. Dev	d (mm)	Std. Dev	d (mm)	Std. Dev	d (mm)	Std. Dev
40	7.9	1.6	7.1	0.2	7.5	0.3	7.0	0.4
55	8.0	0.5	8.8	0.5	8.7	0.4	9.2	0.1
70	12.8	0.4	8.9	0.3	10.0	0.1	9.2	0.5
85	11.3	0.7	11.4	0.2	11.6	0.2	10.8	0.6
100	13.6	0.3	12.3	0.9	12.9	0.8	14.0	0.8
<b>Set (B)</b>								
h (mm)	<b>Cylinder</b>		<b>Cuboid</b>		<b>Triangular Prism</b>		<b>Hexagonal Prism</b>	
	d (mm)	Std. Dev	d (mm)	Std. Dev	d (mm)	Std. Dev	d (mm)	Std. Dev
40	5.4	0.2	5.0	0.2	5.3	0.3	5.4	0.5
55	5.8	0.7	6.2	0.6	6.3	0.3	6.4	0.3
70	7.1	0.6	7.4	0.5	7.5	0.3	7.2	0.3
85	8.2	0.6	8.2	0.3	8.9	0.5	7.8	0.4
100	9.8	1.0	9.9	0.5	9.3	0.3	9.5	0.2
<b>Set (C)</b>								
h (mm)	<b>Cylinder</b>		<b>Cuboid</b>		<b>Triangular Prism</b>		<b>Hexagonal Prism</b>	
	d (mm)	Std. Dev	d (mm)	Std. Dev	d (mm)	Std. Dev	d (mm)	Std. Dev
40	4.3	0.5	4.7	0.2	5.2	0.3	4.8	0.2
55	4.6	0.3	4.9	0.4	5.2	0.3	4.9	0.2
70	5.8	0.2	5.7	0.3	6.6	0.1	5.5	0.4
85	5.7	1.0	6.5	0.1	6.4	1.0	5.7	0.6
100	7.5	0.9	7.6	0.6	7.3	0.3	7.5	1.2
<b>Set (D)</b>								
h (mm)	<b>Cylinder</b>		<b>Cuboid</b>		<b>Triangular Prism</b>		<b>Hexagonal Prism</b>	



	d (mm)	Std. Dev	d (mm)	Std. Dev	d (mm)	Std. Dev	d (mm)	Std. Dev
40	3.8	0.6	3.7	0.4	3.8	0.2	3.5	0.1
55	4.1	0.4	4.4	0.6	3.7	0.5	3.7	0.4
70	4.5	0.1	3.7	0.5	3.8	0.6	3.8	0.3
85	5.1	0.7	5.6	0.2	4.6	0.7	4.9	0.5
100	4.9	0.2	5.9	0.6	5.6	0.8	6.1	1.5

**Statistical study on penetration depth data for various geometries**

The penetration depths of the various projectile geometrics were taken with respect to their release heights. Analysis of Variance (ANOVA) is a method to study and compare the means of the population. In our study, four different projectile shapes are used to study their effects with respect to the penetration depths. Hence, the penetration depth is the response variable with four different factor levels. Since there is only one factor under study, One-Way ANOVA can be used. A few important considerations for performing One-Way ANOVA are:

- i) The categorical variable has to be a fixed factor
- ii) The response variable should be continuous
- iii) Sample size has to be greater than or equal to 15

Minitab 18 was used to statistically analyze the data.

The P value is an important consideration to understand whether there is a difference between the means across each of the sets. **Fig B.1** shows the null and alternative hypothesis used for the study. A significance level of 95% was used, which means that the corresponding inference about the data was true 95% of the time.

## Method

Null hypothesis	All means are equal
Alternative hypothesis	Not all means are equal
Significance level	$\alpha = 0.05$

*Equal variances were assumed for the analysis.*

### SET A

#### Analysis of Variance

Source	DF	Adj SS	Adj MS	F-Value	P-Value
Factor	3	1.028	0.3426	0.37	0.774
Error	56	51.644	0.9222		
Total	59	52.671			

### SET B

#### Analysis of Variance

Source	DF	Adj SS	Adj MS	F-Value	P-Value
Factor	3	0.318	0.1061	0.04	0.990
Error	56	153.208	2.7359		
Total	59	153.527			

### SET C

#### Analysis of Variance

Source	DF	Adj SS	Adj MS	F-Value	P-Value
Factor	3	1.028	0.3426	0.37	0.774
Error	56	51.644	0.9222		
Total	59	52.671			

### SET D

#### Analysis of Variance

Source	DF	Adj SS	Adj MS	F-Value	P-Value
Factor	3	1.028	0.3426	0.37	0.774
Error	56	51.644	0.9222		
Total	59	52.671			

**Figure B. 1.** Analysis of variance for penetration depths of various projectiles in each set used

The P value in all of the cases is greater than the significance level (0.05) and hence the null hypothesis cannot be rejected and all means are equal. Hence, the penetration depth remains the same irrespective of the shape of the projectile.

*Non- Linear Regression analysis:*

The power-law relationship was further evaluated using the non-linear regression to understand its fit and investigate any outliers in the data. Non-linear regression is used when a data cannot be adequately modeled using any linear relationships, i.e., linear, cubic or quadratic. The reason for using this type of regression here is to check the efficiency of the various terms of Equation 13. The projectile length ( $l$ ), release height ( $h$ ) and base surface area of the projectile ( $A$ ) were all studied against the penetration depth ( $d$ ) (Fig B.2 to B.4). Each set of figures consists of the fit line plot equation, which related the two terms in the x and y axes, respectively. In most of cases, the power-law relationship was valid as the fitted plot agreed with the data. One of the limitations arose because the data points were limited and therefore, even one outlier might have a significant effect on the model.

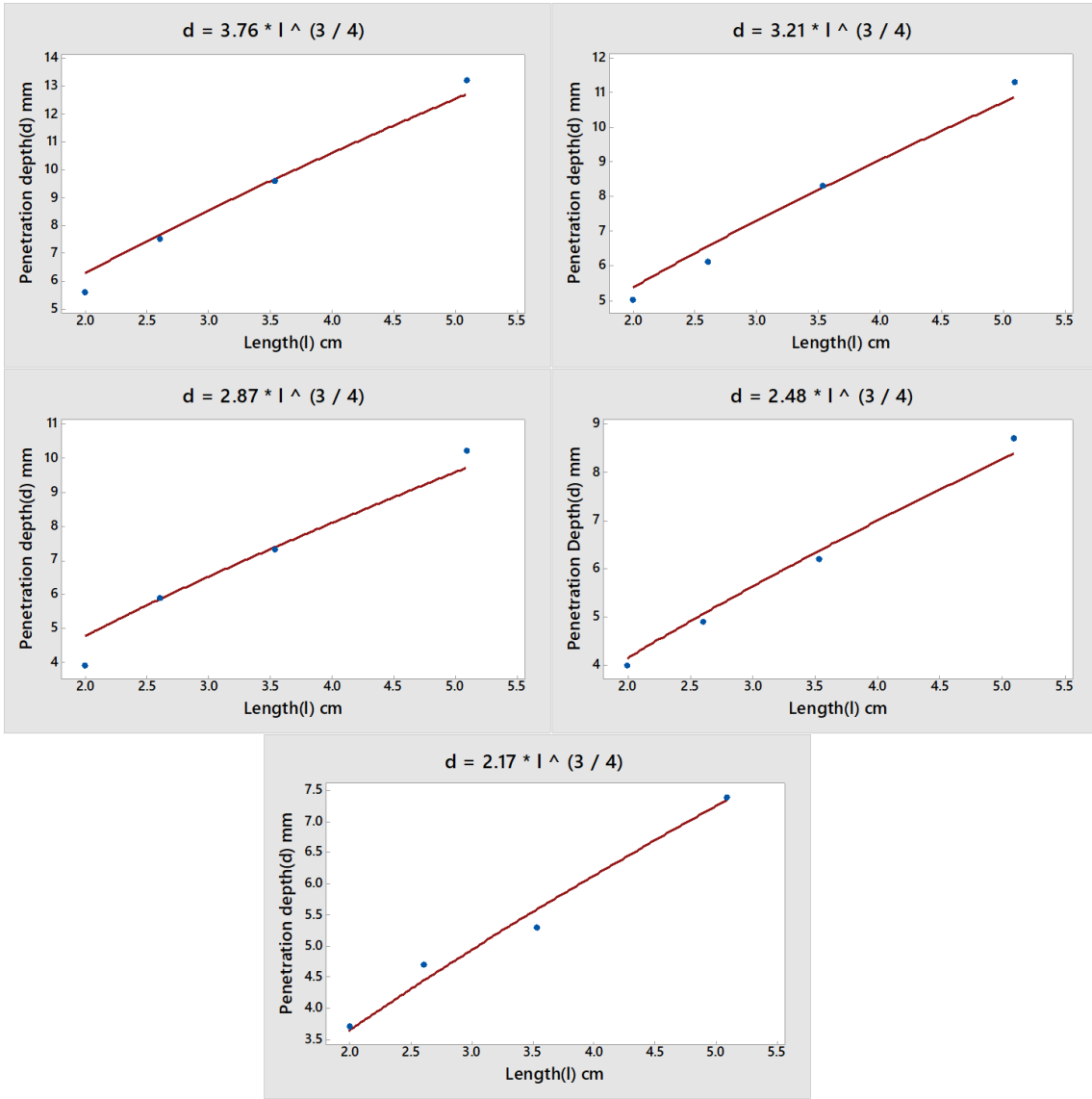


**Figure B. 2.** Fitted line plots of penetration depth as a function of length of the projectile for all release heights used.

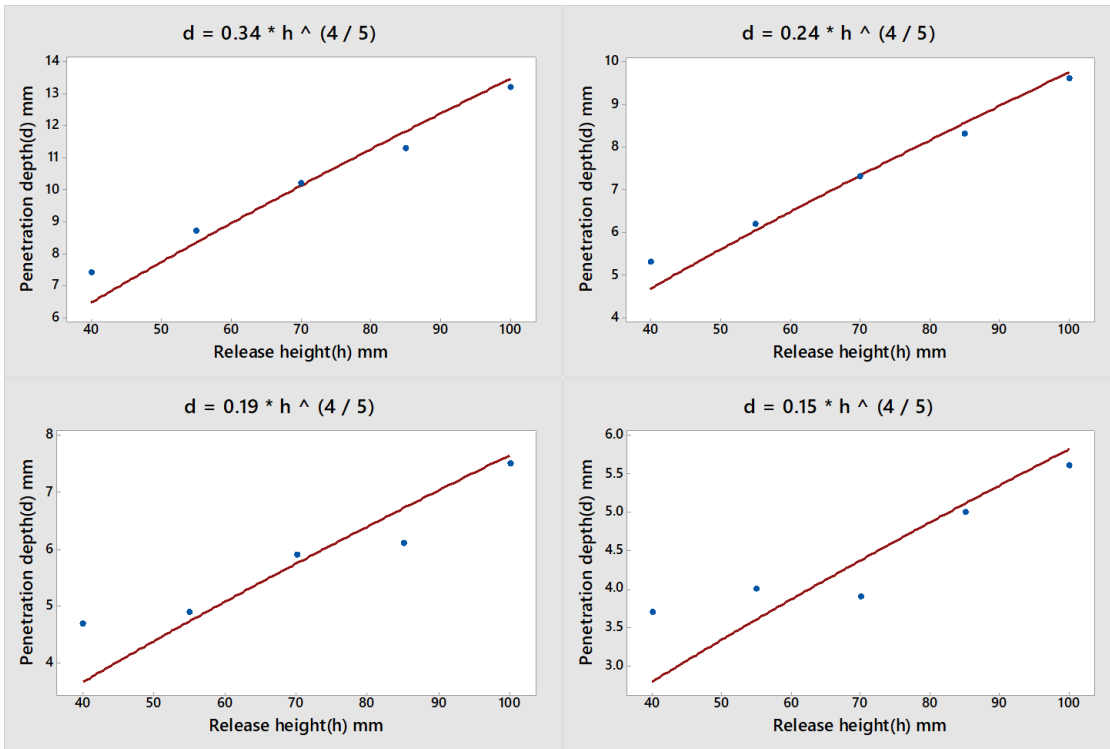


**Figure B. 3.** Fitted line plots of penetration depth as a function of release height of the projectile for each set.

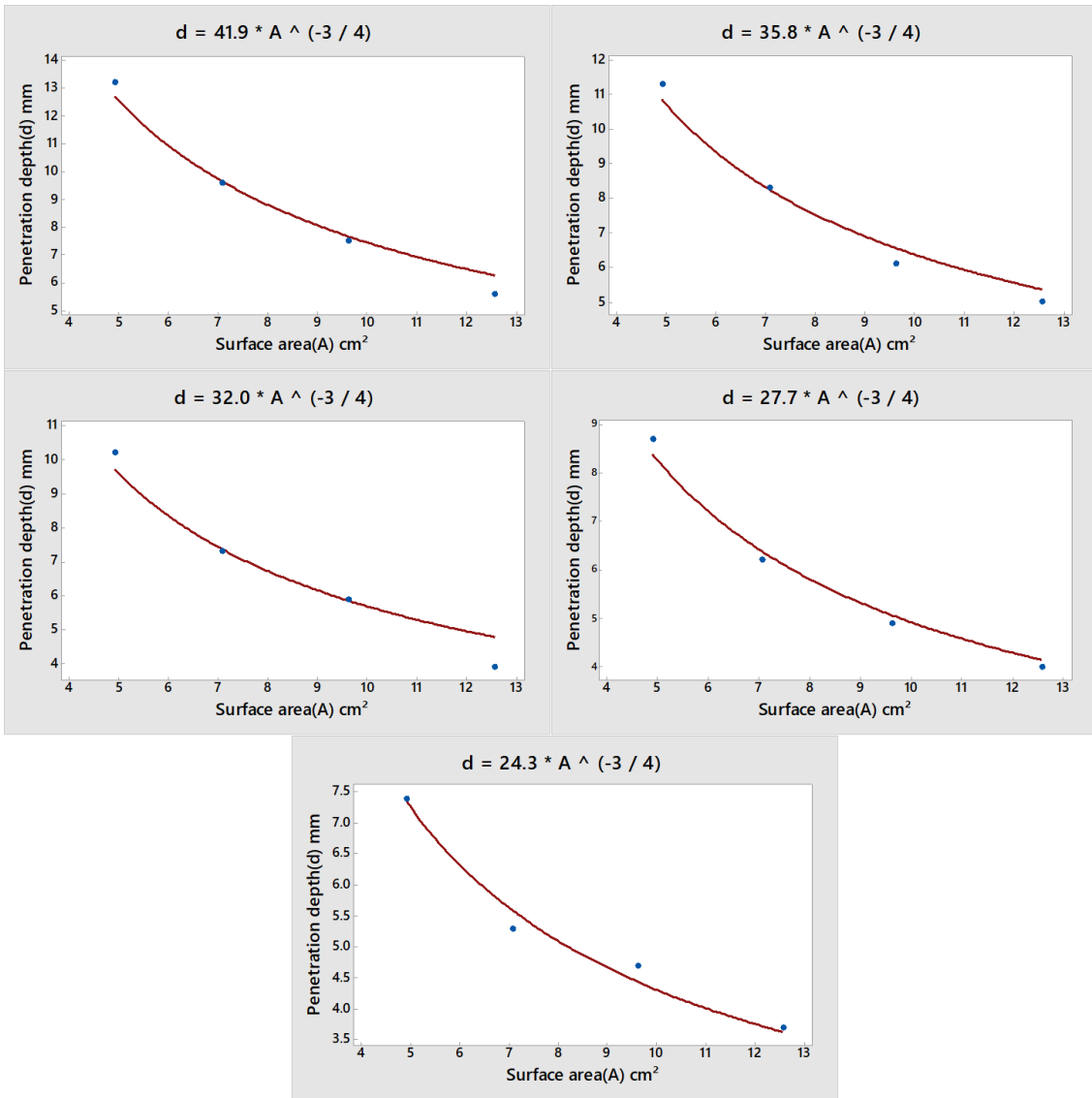


**Figure B. 4.** Fitted line plots of penetration depth as a function of surface area of the projectile for all the release heights used